A circular zone of attachment to the extracellular matrix provides directionality to the motility of *Toxoplasma gondii* in 3D

Rachel V. Stadler[1], Shane R. Nelson[2], David M. Warshaw[2], Gary E. Ward[1]*

[1] Department of Microbiology and Molecular Genetics, and
[2] Department of Molecular Physiology and Biophysics,
University of Vermont Larner College of Medicine, Burlington, Vermont, U.S.A. 05405

* Correspondence to: Gary.Ward@uvm.edu

Abstract

Toxoplasma gondii is a protozoan parasite that infects 30-40% of the world's population. Infections are typically subclinical but can be severe and, in some cases, life threatening. Central to the virulence of *T. gondii* is an unusual form of substrate-dependent motility that enables the parasite to invade cells of its host and to disseminate throughout the body. A hetero-oligomeric complex of proteins that functions in motility has been characterized, but how these proteins work together to drive forward motion of the parasite remains controversial. A key piece of information needed to understand the underlying mechanism(s) is the directionality of the forces that a moving parasite exerts on the external environment. The linear motor model of motility, which has dominated the field for the past two decades, predicts continuous anterior-to-posterior force generation along the length of the parasite. We show here using three-dimensional traction force mapping that the predominant forces exerted by a moving parasite are instead periodic and directed in towards the parasite at a fixed circular location within the extracellular matrix. These highly localized forces, which are generated by the parasite pulling on the matrix, create a visible constriction in the parasite's plasma membrane. We propose that the ring of inward-directed force corresponds to a circumferential attachment zone between the parasite and the matrix, through which the parasite propels itself to move forward. The combined data suggest a closer connection between the mechanisms underlying parasite motility and host cell invasion than previously recognized. In parasites lacking the major surface adhesin, TgMIC2, neither the inward-directed forces nor the constriction of the parasite membrane are observed. The trajectories of the TgMIC2-deficient parasites are less straight than those of wild-type parasites, suggesting that the annular zone of TgMIC2-mediated attachment to the extracellular matrix normally constrains the directional options available to the parasite as it migrates through its surrounding environment.

Introduction

Parasites of the phylum Apicomplexa cause pervasive human disease and are responsible for approximately one million deaths annually [1, 2]. *Toxoplasma gondii* is the most prevalent apicomplexan parasite, infecting 30-40% of the human population worldwide [3-5]. *T. gondii* infections are typically subclinical in immunocompetent individuals but may cause blindness [6, 7]. In immunocompromised individuals and the developing fetus, the disease can be life-threatening [5, 8, 9].

T. gondii is a single-cell protozoan, and the pathogenesis associated with acute infection is caused by the highly motile tachyzoite life-cycle stage. Like other apicomplexan parasites, the *T. gondii* tachyzoite uses a unique form of substrate-dependent motility to invade into and egress from cells of its host, to migrate across biological barriers, and to disseminate throughout the infected host. Motility is, therefore, central to the pathogenesis of toxoplasmosis [10-12]. The parasite has no cilia or flagella and can move at speeds of up to 3 μm/s without the leading edge protrusions that drive the substrate-dependent motility of other eukaryotic cells. Within a three-dimensional (3D) extracellular matrix, the parasite moves along a complex helical trajectory characterized by regular oscillations in velocity and changes in trajectory curvature and torsion [13].

Motility is driven, at least in part, by a complex of proteins known as the glideosome, which is anchored to the inner membrane complex at the parasite periphery (Figure 1A). In the "linear motor" model of motility, short actin filaments are bound through the bridging protein TgGAC to the cytosolic tails of transmembrane adhesins, such as TgMIC2, and translocated towards the posterior end of the parasite via a class XIV myosin, TgMyoA [14-17]. If the extracellular domains of the transmembrane adhesins are attached to ligands on the substrate, the rearward translocation of actin results in forward movement of the parasite. Other apicomplexan parasites, including those that cause malaria (*Plasmodium spp.*) and cryptosporidiosis (*Cryptosporidium spp.*), express similar glideosome proteins, suggesting that the mechanism of motility is conserved [18].

Although abundant evidence supports the importance of TgMyoA and other components of the glideosome in motility [12, 16, 19-23], several recent observations have raised questions about whether these proteins generate force as described by the linear motor model and, if so, whether this is the only motility mechanism available to the parasite [19, 24-28]. Because parasite motility is essential for virulence, elucidation of the mechanism(s) underlying motility is of both fundamental cell biological interest and potential clinical relevance. One key piece of missing information needed for a full mechanistic understanding of motility is the directionality of the forces the parasite exerts on the external environment as it moves along its 3D helical trajectory. The linear motor model predicts continuous anterior-to-posterior forces along the entire periphery of the moving parasite. We show here using 3D traction force mapping that the predominant forces exerted by the parasite are instead organized into a

71 highly localized circumferential ring of inward-directed force at a fixed location within the matrix. These
72 inward-directed forces create a visible constriction of the parasite's plasma membrane, reflecting a
73 circular zone of tight attachment of the parasite to the matrix through which the parasite passes through as
74 it progresses forward along its helical trajectory. In the absence of this circular attachment zone, the
75 parasite is still able to move but this movement loses much of its directionality.
76
77 **Results**
78
79 **Development of a quantitative 3D traction force mapping assay**
80 As a first step towards visualizing the forces exerted by parasites moving in 3D, we used a bead
81 displacement assay in the well-established Matrigel extracellular matrix model [13, 27, 29]. Fluorescent
82 microspheres embedded within the Matrigel were pulled towards a moving parasite from nearby anterior,
83 posterior, and lateral locations within the matrix, and these microspheres returned to their original
84 positions after the parasite had passed (Figure 1B, Videos 1&2). These results demonstrate that the
85 parasite does indeed exert a detectable force on the surrounding matrix. Unexpectedly, we also noted
86 constrictions in the body of the fluorescent parasite as it moved (Video 2). These constrictions were even
87 more apparent by brightfield microscopy (Figure 1C, Video 3). Each constriction formed at the apical end
88 of the parasite and remained stationary relative to the matrix as the parasite moved through, reminiscent
89 of the "moving junction" through which the parasite penetrates during host cell invasion (discussed
90 further below).
91 To develop a more quantitative force mapping assay and explore the relationship between the
92 constrictions and matrix deformation, we used Alexa-Fluor 647-conjugated fibrinogen [30] to generate a
93 fluorescent 3D fibrin matrix (Figure 2A and Video 4). The use of a fluorescent matrix enabled mapping of
94 matrix displacements at all spatial points in our imaged volume rather than at the limited number of
95 discrete positions offered by fluorescent microspheres. Parasite motility in matrices generated using 2.25
96 mg/ml fibrinogen was indistinguishable from that observed in Matrigel (Figure 2B and Suppl. Figure 1A-
97 B). Visual comparison of successive image volumes confirmed that parasites moving through fluorescent
98 fibrin also deform the matrix (Figure 2C and Video 5) and undergo constrictions (see below) similar to
99 those observed in Matrigel.
100 To calculate and map the deformations of the fluorescent fibrin matrix, we used the Fast Iterative
101 Digital Volume Correlation (FIDVC) algorithm developed by Christian Franck's group
102 (https://github.com/FranckLab/FIDVC) to iteratively determine the 3D fibrin displacement fields between
103 consecutive volumetric image stacks in our time series [31]. Each image volume is divided into 16,807
104 subvolumes (49 x 49 x 7 subvolumes in x, y, z). The algorithm compares the voxel intensity pattern

between corresponding subvolumes at two consecutive timepoints, calculating one 3D displacement vector per subvolume. The data can be displayed as a map for the entire imaging volume or for any 2D plane (*x-y*, *x-z*, or *y-z*; see Video 6). Most of the 2D images below show the displacement maps in the *x-y* plane on one of the seven *z* subvolume levels.

To filter out background noise and identify displacements caused by the parasite, we calculated displacement vectors during periods when no parasites were moving within our imaging volume and used these to establish a displacement detection threshold for each dataset (see Methods and Figure 3 for details). Using this approach, the limit of detection for 3D displacement magnitudes in the system ranges from 42 - 46 nm; a similar 3D displacement detection threshold (43 - 46 nm) was observed in samples containing no parasites (see Figure 6E below), validating the approach. When analyzing data in the *x-y* plane only, the background cutoff was calculated using the *x-y* displacement magnitudes (rather than the *x-y-z* displacement magnitudes); this lowered the displacement detection threshold to 28 - 31 nm.

In order to translate matrix displacements into the magnitude of forces generated by the parasite, we determined the viscoelasticity of the fibrin matrix using laser trapping (see Methods). The fibrin gel behaves as a predominantly elastic matrix (Suppl. Figure 2) with an elastic modulus of 15.6 pN/µm and a viscous modulus of 0.09 pN*s/µm. The minimal detectable force magnitude in this system is therefore 0.66-0.72 pN in 3D and 0.45-0.49 pN in the *x-y* plane.

Parasite constrictions are tightly linked to periodic bursts of matrix deformation and motility

With this system for 3D traction force mapping in hand, we analyzed the pattern and directionality of forces produced by wild-type parasites as they moved through the fibrin matrix. Plotting fibrin displacement as *x-y* maps showed that the matrix deforms in towards the parasite from all *x-y* directions at discrete, periodic time points along the trajectory, before relaxing back to its initial position (*e.g.*, Figures 4A-D and Videos 7, 8). Viewing the data as projections along each axis demonstrates that the matrix is simultaneously pulled in towards the parasite in all three dimensions (Suppl. Figure 3 and Video 6). In approximately 50% of cases, inward deformation occurred between two consecutive image volumes (1.6 seconds apart) and was followed in the next image volume by relaxation (*e.g.*, Figure 4A-C). In most other cases, the inward deformation was held through multiple time points before relaxing (Suppl. Figure 4). During periods of motility when the matrix was not being pulled inward or relaxing outward, little deformation of the matrix above background was detectable (*e.g.*, Figure 4C, leftmost and rightmost panels). This observation suggests either that the parasite pulls on the matrix only during some portions of its trajectory or that the parasite produces both strong and weak deformations, and the weak deformations – which could be continuous – are below our level of detection.

When the displacement maps were overlaid onto the images of the moving parasites, it was immediately apparent that the timing of each large matrix deformation coincided with the presence of a parasite constriction and that the displacement vectors pointed primarily in towards the constriction (Figure 4C, D; additional examples are shown in Suppl. Figure 5). The fact that the displacements were directed inwards rather than away from the parasite indicates that the pinching of the parasite membrane results from pulling forces generated by the parasite rather than the parasite squeezing through a narrow pore within the matrix, which would push the matrix away. When a constriction persisted over multiple time points, the fibrin continued to deform into the constriction and/or to hold the deformation over those same time points as the parasite passed through (*e.g.*, Figure 4D).

The time it took a parasite to move completely through a constriction ranged from 1.6-56.2 seconds (average 6.8 ± 5.2 seconds, measured in brightfield; n=99 parasites, 188 constrictions) with the longer times due to a stall in forward progression of a constricting parasite. The time between one constriction finishing and another beginning was also variable (Figure 5A). In 46% of the cases, the end of one constriction was followed immediately by the beginning of another, while in 14% of the cases a second constriction would start before the first constriction finished (Figure 5A, B and Video 9). Most importantly, all parasites that move at least one body length undergo a constriction and the total trajectory length is directly proportional to the number of constrictions observed (Figure 5C), strongly suggesting that the parasite-generated forces that create the constriction play an important role in forward movement.

The much reduced width of a constricting parasite (2.6 ± 0.4 μm *vs.* 1.4 ± 0.2 μm at the parasite's widest point before and during a constriction, respectively; Figure 5D, n=15 parasites, 19 constrictions) led us to question whether the constriction presents a physical obstacle to the forward motion of the nucleus (normal nuclear diameter measured by DNA staining = 2.0 ± 0.3 μm). In parasites labeled with both a fluorescent DNA stain and a fluorescently-labeled antibody against the major surface protein, TgSAG1 (to visualize the constriction), the normally round parasite nucleus did indeed become thinner and more elongate as it passed through the constriction and regained its round shape once it was through (Figure 5E). The ratio of the nuclear dimensions perpendicular and parallel to the long axis of the parasite was 0.93 ± 0.08 in a non-constricting parasite and 0.50 ± 0.06 during a constriction (n=9 parasites, 15 constrictions).

Interestingly, the distribution of the fluorescent anti-TgSAG1 antibody on the parasite surface changed as the parasite moved: much of the fluorescent signal appeared to be "swept" from anterior to posterior at the constriction as the parasite moved through (Suppl. Figure 6 and Video 10). The redistributed antibody was ultimately shed and deposited behind the moving parasite in the form of a fluorescent helical trail within the Matrigel (Suppl. Figure 6 and Video 10).

172 **Parasites that do not generate constrictions do not detectably deform the matrix**

173 Since TgMyoA is thought to play a central role in force production during parasite motility (Figure
174 1A), we conducted force mapping experiments using a parasite line lacking TgMyoA [20]. As previously
175 reported [27], these parasites are much less motile in 3D than wild-type parasites: only 18 of 769
176 TgMyoA knockout parasites examined (2%) moved one body length or more during a 302-second time
177 course, compared to 99 of 278 wild-type parasites (36%). Of the 18 TgMyoA knockout parasites that
178 moved at least one body length, none showed clear constrictions at a fixed point within the matrix like
179 those seen in wild-type parasites (Figure 6A). The pattern of movement was also different from wild-type
180 parasites; rather than moving along smooth helical trajectories, the TgMyoA knockout parasites moved in
181 tightly twisting arcs or in a stair-like pattern consisting of right-angled turns associated with a sharp bend
182 in the body of the parasite (Figure 6A and Video 11). In stark contrast to the wild-type parasites, we also
183 saw no evidence by traction force mapping of a ring of inward-directed forces produced by the TgMyoA
184 knockout parasites. In fact, we did not detect any displacement of the matrix above background noise by
185 these parasites (Figure 6B and Suppl. Figure 7, n=16 parasites), suggesting that any forces produced by
186 the moving knockout parasites are below the limit of detection in our traction force assay.

187 We also tested whether the surface adhesin, TgMIC2, plays a role in generating the constriction-
188 associated inward forces on the matrix. The motility defect in parasites lacking TgMIC2 [29] is less
189 severe than the defect in parasites lacking TgMyoA, with 36 of 297 TgMIC2 knockout parasites (12%)
190 capable of moving more than one body length (see also [29, 32]). However, these parasites often moved
191 in an erratic, stop and start pattern, bending sharply and moving in tightly twisting arcs (Figure 6A and
192 Video 12). The TgMIC2 knockout parasites also failed to form constrictions and did not detectably
193 deform the fibrin matrix (Figure 6C, n=36 parasites, Suppl. Figures 8A-C, n=18 parasites) despite being
194 able to move at maximum speeds similar to wild-type parasites [29]. Taken together, these data confirm
195 that motility is significantly altered, but not completely eliminated, in parasites lacking TgMyoA or
196 TgMIC2. Furthermore, the data demonstrate that both proteins are required to produce the constriction
197 and the constriction-associated inward forces on the matrix observed during the motility of wild-type
198 parasites.

199

200 **TgMIC2-deficient parasites move less directionally**

201 The larger number of TgMIC2 knockout parasites capable of long runs of motility (compared to the
202 MyoA knockouts) enabled us to analyze their phenotype in greater detail. The nuclei of parasites lacking
203 TgMIC2 did not change shape as they moved in 3D (Figure 7A and Suppl. Figure 8D), providing further
204 evidence that these parasites do not undergo the constrictions seen in wild-type parasites. Given their
205 apparent propensity for tight turns, we also quantified the ability of the TgMIC2 knockout parasites to

206 move directionally, by comparing displacement distance (first to last point) to total trajectory length.
207 While parasites with and without TgMIC2 traveled along trajectories of similar mean length (38 ± 9 μm
208 vs. 42 ± 8 μm, respectively), parasites lacking TgMIC2 moved approximately half as far from their
209 starting point as wild-type parasites (Figure 7B and Suppl. Figure 8E). These data suggest that the
210 circumferential zone of attachment to the matrix, which requires TgMIC2, functions to convert
211 meandering motility into more linear, directed forward progression.
212
213 **Discussion**
214 The linear motor model of apicomplexan motility predicts that a parasite moves by pulling
215 continuously on the matrix in an anterior-to-posterior direction along the length of the parasite. It was,
216 therefore, unexpected that the predominant forces revealed by our new 3D traction force mapping assay
217 were instead periodic and highly localized, pointing inwards from all directions towards a circumferential
218 location on the parasite surface. This annular band of parasite-generated, inward-directed force forms at a
219 fixed position within the matrix and creates a visible constriction at the parasite periphery. The
220 constriction passes from the anterior to the posterior end of the parasite as the parasite moves forward.
221 Typically, when the constriction reaches the parasite's posterior end a new constriction forms at the apical
222 end and the cycle repeats. These results suggest that the moving parasite periodically assembles ring-
223 shaped zones of tight attachment to the matrix, which deform the matrix and serve as stationary platforms
224 that the parasite propels itself through, one body length at a time.
225 **Attachment to the substrate, force generation, and motility in 2D *vs.* 3D.** Both malaria
226 sporozoites and *T. gondii* tachyzoites are capable of moving in circles on 2D surfaces. The pioneering
227 work of Munter, Frischknecht and colleagues combined traction force mapping with reflection
228 interference contrast microscopy (RICM) during the 2D circular gliding of malaria sporozoites [33]. They
229 concluded that the parasite adheres to the substrate at its apical and posterior ends; each of these adhesion
230 sites produces stalling forces parallel to the long axis of the parasite, and disengagement of the adhesion
231 sites drives forward motion. Traction forces perpendicular to the direction of movement were also
232 detected at the center of the parasite but these were interpreted as nonspecific and nonproductive. The
233 apical and posterior adhesion sites were shown to move forward *with* the parasite, rather than remaining
234 stationary with respect to the substrate.
235 *T. gondii* tachyzoites demonstrate a second form of productive motility on 2D surfaces called helical
236 gliding: the banana-shaped parasite starts with its left side in contact with the substrate, moves forward
237 one body length while rotating along its longitudinal axis until it lies on its right side, and then flips back
238 to its left side to repeat the cycle [34]. This form of motility is the equivalent of the fully helical
239 trajectories seen in 3D but constrained in 2D by contact of the curved parasite with the rigid substrate. In

240 RICM studies of 2D helical gliding [21, 35] the tachyzoite was seen to first attach to the substrate at its
241 apical end. The zone of attachment then expanded along the length of the parasite and, as the parasite
242 moved forward and its apical end twisted up off the cover slip, the zone of attachment shrunk until it was
243 reduced to a spot at the posterior end. In contrast to *Plasmodium* sporozoites, the position of the
244 tachyzoite adhesion site remained fixed relative to the substrate and the parasite slid over this attachment
245 site as the parasite moved forward. 2D traction force mapping revealed forces parallel, but not
246 perpendicular, to the longitudinal axis of the tachyzoite; these traction forces, together with spring-like
247 forces generated by the parasite's microtubule cytoskeleton, were postulated to produce forward motion
248 [35].
249 When these previous studies of *T. gondii* 2D motility are combined with the 3D results presented
250 here, a consensus emerges that the basic unit of motility consists of apical attachment to the substrate,
251 followed by apical-to-posterior translocation of the adhesion site, which is fixed in its position relative to
252 the substrate. When the adhesion site reaches the posterior end of the parasite, a new apical attachment
253 site is formed, and the cycle begins again. The adhesion site in a 3D matrix is circular, and the pulling
254 forces exerted by the parasite on the matrix manifest as a visible constriction in the parasite's plasma
255 membrane. In 2D, no deformation of the parasite has been reported at the adhesion site, likely reflecting
256 differences in attachment to the substrate via a point/patch on the parasite surface *vs.* circumferential
257 attachment. We also saw no evidence in 3D for a persistent stall force at the rear of the parasite. The
258 biggest difference between the 2D and 3D force mapping data is that, in 3D, all force vectors point
259 towards one highly localized circumferential region on the surface of the parasite, and many of these
260 force vectors contained a strong component perpendicular to the long axis of the parasite.
261 Munera Lopez et al [36] also recently noted that tachyzoites show constrictions as they move through
262 Matrigel. These authors ascribed the constrictions to the parasite having to squeeze through small pores in
263 the matrix. Our force mapping results and the regularity with which the constrictions form at the apical
264 end of the parasite argue strongly that the constrictions do not result from the parasite pushing its way
265 through pores, but rather from parasite-generated pulling forces on the matrix. Annular constrictions that
266 remain stationary relative to the surrounding environment have also previously been reported along the
267 length of *Plasmodium* ookinetes as they move through peritrophic membrane and microvillar network of
268 the mosquito midgut [37-39], suggesting that parasite-generated circular zones of attachment to the
269 environment may be a conserved feature of apicomplexan motility in 3D.
270 **3D motility and invasion: variations on a theme.** During the invasion of host cells by *T. gondii* and
271 other apicomplexan parasites, proteins secreted from the parasite's apical organelles assemble a ring-
272 shaped zone of tight attachment between the membranes of the two cells. This "moving junction" does
273 not in fact move: it is anchored to the host cytoskeleton and is hypothesized to provide a fixed platform

274 against which the parasite exerts force [40-45]. Parasite surface adhesins, which are engaged with the
275 junction via their extracellular domains, are thought to be translocated by MyoA in an anterior-to-
276 posterior direction, pushing the parasite through the junction and into the host cell. The body of the
277 parasite narrows dramatically as it passes through the moving junction, bearing a striking resemblance to
278 the constrictions seen during 3D motility.

279 Two central players in moving junction formation in *T. gondii* are TgAMA1, an adhesin secreted onto
280 the parasite surface from the micronemes, and TgRON2, which is secreted by the parasites into the host
281 cell plasma membrane and serves the ligand to which TgAMA1 binds. Neither TgAMA1 [46, 47] nor
282 TgRON2 (RVS and GEW, unpublished data) plays any detectable role in parasite motility. Instead,
283 TgMIC2 – another microneme protein secreted onto the parasite surface – likely plays an analogous role
284 during motility to that of TgAMA1 during invasion, with TgMIC2 binding to ligands in the extracellular
285 matrix rather than to TgRON2 in the host cell membrane.

286 As the parasite moves forward during both invasion and 3D motility, it simultaneously rotates around
287 its long axis [13, 34, 48]. Our results provide a possible explanation for this rotational motion. In both
288 cases, parasite receptors bind to their cognate ligands in the form of a circular ring of attachment that is
289 fixed in position relative to the host cell (in the case of invasion) or the extracellular matrix (in the case of
290 3D motility). It has long been proposed that the TgMyoA motor driving invasion and motility is arranged
291 helically within the parasite, along the spiraling subcortical microtubules (*e.g.*, [35]). Alternatively, a
292 recent modeling study suggests that the unique geometry of the parasite periphery can generate a self-
293 organized helical pattern of anterior-to-posterior actin flow [49]. In either case, if the actin filaments flow
294 helically and are connected to the tails of transmembrane adhesins engaged circumferentially with the
295 host cell surface or extracellular matrix, the forward motion of the parasite either into the cell or through
296 the matrix will by definition be accompanied by rotational twist. Some portion of the perpendicular force
297 that we observed directed towards the annular constriction in our traction force assays may in fact reflect
298 torque on the matrix produced by the parasite as it twists through this circular zone of attachment.

299 As a parasite invades a host cell, antibodies are "shaved" off the parasite surface at the moving
300 junction by an as yet unknown mechanism [50]. Remarkably, a similar phenomenon is observed during
301 3D motility: fluorescent antibody against the surface protein TgSAG1 is lost from the parasite surface
302 anterior to the constriction and shed as a helical trail of fluorescence behind the moving parasite (Suppl.
303 Figure 6 and Video 10).

304 The numerous parallels between invasion and 3D motility noted here suggest that the two processes
305 may be more mechanistically similar than previously recognized [14, 21], with implications for our
306 understanding of each. For example, our data suggest that 3D motility can be best described as the
307 parasite undergoing sequential invasion-like events through circular zones of attachment to the matrix;

308 during invasion the parasite only needs to move a single body length to penetrate into the host cell, but
309 during motility the parasite can string multiple constriction events together to move multiple body lengths
310 (Figure 5C). The data also raise the possibility that the characteristic constriction of the parasite seen at
311 the moving junction during invasion does not reflect the parasite being squeezed as it *pushes* itself
312 through the small diameter opening into the host cell, as is commonly thought (*e.g.,* [51, 52]), but rather
313 the parasite attaching to and *pulling* on the host cell plasma membrane as it penetrates.

314 **The linear motor model.** The data presented here with wild-type parasites are at least partially
315 consistent with the linear motor model of motility, in which: (a) actin polymerization is nucleated at the
316 apical tip of the parasite by formin1 [21]; (b) TgMyoA translocates the actin filaments in an anterior-to-
317 posterior direction along the length of the parasite; and (c) binding of the rearward flowing actin filaments
318 to transmembrane adhesins [16], whose extracellular domains are attached to the substrate, drives the
319 forward motion of the parasite (Figure 1A). While anterior-to-posterior actin flux may occur along the
320 entire length of the parasite periphery [49, 53, 54], we propose a modification to the linear motor model
321 in which force is generated, in whole or in part, by the rearward translocation of the subset of actin
322 filaments that are coupled to adhesins at the circular ring of attachment. We were unable to detect any
323 anterior-to-posterior bias in the force vectors at the constriction, which would be expected if the parasite
324 pulls against this zone of attachment in order to move forward. These forces may be below our limit of
325 detection (~0.72 pN). Alternatively, compression of the fibrin immediately adjacent to the constriction
326 might increase the local elastic modulus of the matrix, making it more difficult to see proximal
327 displacements because of a local increase in the displacement detection threshold. Because the fibrin gel
328 behaves primarily as an elastic matrix (Suppl. Figure 2), the relationship between acceleration and force is
329 complex and we cannot calculate with any confidence how much total displacement / force would be
330 required to achieve a given parasite velocity and relate this to the displacement detection threshold of the
331 assay.

332 The regularity with which the parasite generates the circular zones of attachment on its surface,
333 yielding on average one constriction per body length of motion (Figure 5D), could be due to periodic
334 bursts of formin1-mediated actin polymerization at the parasite's apical tip [21] or to periodic release of
335 adhesins such as TgMIC2 from the micronemes. Alternatively, the observation that constrictions occur
336 back-to-back almost 50% of the time (Figure 5A), may suggest that a new constriction forms at the apical
337 tip before the prior constriction has ended, but this new constriction stalls as the TgMyoA (or possibly
338 TgMyoH [21]) to which it is connected pulls against the adhesive forces of the more posterior previous
339 constriction. Future real-time analysis of actin polymerization and microneme secretion in motile
340 parasites, together with higher sensitivity force mapping, will be necessary to further interrogate the
341 periodic nature of ring assembly.

342 The lack of a motility-associated constriction in TgMyoA-deficient parasites could reflect an
343 inability either to assemble ring of adhesins at the apical tip of these parasites or, more likely, to move
344 through the incipient ring once it has formed. Alternatively, it could be that the ring-shaped structures that
345 form during motility are contractile, and contractility requires TgMyoA. The inward deformation of the
346 fibrin matrix towards the constriction reported here is consistent with a contractile ring, as is the physical
347 constriction of the parasite plasma membrane. Intriguingly, the speed of the parasite's forward motion
348 increases once the constriction passes the halfway point on the parasite's longitudinal axis (Suppl. Figure
349 9, n=20 parasites, 24 constrictions). This observation suggests that physical squeezing of the tapering
350 posterior end of the parasite by the narrow (and potentially contractile) constriction may contribute to the
351 parasite's forward motion.
352 If the coupling of actin flow to the circular zone of attachment is important for forward motion, how
353 do the parasites lacking TgMIC2 that move do so at near normal speeds [29] in the absence of
354 constrictions? First, it is possible that both the wild-type and mutant parasites generate small forces
355 distributed over their entire surface (in addition to larger forces that may be generated at the constriction
356 in wildtype), which are collectively sufficient to drive motility but individually below our level of
357 detection. Alternatively, the loss of TgMyoA or TgMIC2 might lead to compensatory changes in the
358 expression of other genes with overlapping or redundant function [25, 55, 56]. The TgMIC2 KO parasites
359 do in fact show changes in the expression of several other microneme and motility-associated proteins
360 [29]. Finally, it is possible that parasites lacking TgMyoA and/or TgMIC2 use a motility mechanism that
361 is entirely different from that of wild-type parasites (*e.g.*, [20, 24]) and does not involve a constriction but
362 is nevertheless capable of supporting motility and sustaining the parasite's lytic cycle. By analogy with
363 observations from animal cells [57], parasites might use different mechanisms for motility in different
364 situations such as squeezing through tight junctions [10] *vs.* migrating through loose interstitial tissues. If
365 the motility of the mutants is driven by a different mechanism than that of wild-type parasites, higher
366 sensitivity 3D traction force mapping may reveal informative differences in their pattern of force
367 generation.
368 **A guidance system for motility?** The forward motion of the TgMIC2 knockout parasites, which
369 lack the circular attachment zone, is significantly more disorganized than the motility of wild-type
370 parasites. The mutant parasites can still generate relatively long trajectories, but the trajectories take them
371 less far from their starting point than wild-type parasites. As discussed above, attachment to the matrix via
372 a circular ring of adhesion likely contributes to the rotational twisting of the parasite as it moves forward
373 and thereby to the helicity of the parasite's trajectory. Extensive studies of the helical swimming behavior
374 of bacteria has shown that a curved cell shape and helical trajectory are a particularly efficient way for
375 small cells to move through viscous media [58-62]. Engagement of *T. gondii* with the extracellular matrix

through a circular band of adhesion may therefore not only create a fixed platform for the parasite to pull against and move forward; it may also function as part of a guidance system to help the parasite move efficiently through the various environments it encounters as it disseminates through the tissues of the unfortunate organisms it infects.

Methods

Parasite and Cell Culture. Parasites were propagated by serial passage in human foreskin fibroblasts (HFFs). HFFs were grown to confluence in Dulbecco's Modified Eagle's Medium (DMEM) (Life Technologies, Carlsbad, CA) containing 10% (vol/vol) heat-inactivated fetal bovine serum (FBS) (Life Technologies, Carlsbad, CA), 10 mM HEPES pH 7, and 100 units/ml penicillin and 100 ug/ml streptomycin, as previously described [63]. Prior to infection with *T. gondii*, the medium was changed to DMEM supplemented with 10mM HEPES pH 7, 100 units/ml penicillin and 100 ug/ml streptomycin, and 1% (vol/vol) FBS.

Pitta Chamber Assembly. 22×22 coverglasses were washed with Alconox detergent, rinsed with tap water, deionized water, and ethanol (100%), and air dried. Two strips of double-sided tape (Scotch 3M, St. Paul, MN) were placed 3 mm apart on a glass slide, and the coverglass was placed on top of the tape and pressed firmly to ensure a complete seal. The flow cell volume was approximately 10 µl.

Matrigel Matrix. Pitta chambers containing parasites embedded in polymerized Matrigel were prepared as previously described [13]. Briefly, parasites were harvested from infected HFFs via syringe release and passed through a 3 µm Nucleopore filter (Whatman, Piscataway NJ). Parasites were pelleted and resuspended at in Live Cell Imaging Solution (LCIS) buffer. For fluorescence imaging, the LCIS contained 0.5 mg/ml Hoechst 33342 (Thermo Scientific, Waltham, MA) and/or a 1:20 dilution of Alexa546-conjugated anti-TgSAG1 (see Table 1). Fluorescent anti-TgSAG1 (100µg) was prepared using the Alexa Fluor 546 Antibody Labeling Kit (Thermo Scientific, Waltham, MA) as per the manufacturer's instructions. Parasites were incubated with the Hoechst 33342 (10 minutes) and/or anti-TgSAG1(15 minutes) at room temperature, then mixed with Matrigel and LCIS on ice in a 1:3:3 (vol/vol/vol) ratio and immediately added to a Pitta chamber. The Pitta chamber was incubated for three minutes at 35°C in a custom-build heated microscope enclosure (UVM Instrumentation and Model Facility, Burlington, VT) before imaging.

410 **Fibrin Matrix.** Unlabeled and Alexa-Fluor 647-labeled fibrinogen (both from Thermo Scientific,
411 Waltham, MA) were each dissolved in 0.1M sodium bicarbonate (pH 8.3) to 15 mg/ml. Aliquots of 50 µl
412 were flash frozen and stored at -80C until use. Fibrin gels [30] containing parasites were prepared in Pitta
413 chambers as follows. The parasite culture medium was replaced with LCIS buffer before harvesting via
414 syringe release and filtering. 500 µl of the parasite suspension were pelleted and resuspended in LCIS
415 buffer to achieve a higher parasite concentration. Parasites were mixed with fibrinogen (final fibrinogen
416 concentration of 2.25, 4.5, or 9 mg/ml). LCIS buffer containing thrombin (Sigma, Burlington, MA) and
417 FBS was added to the parasite-fibrinogen suspension for final concentrations of $1.5x10^8$ parasites per ml,
418 1 unit/ml of thrombin, and 10% FBS. The mixture was immediately pipetted into a Pitta chamber and
419 allowed to polymerize at room temperature for three minutes before mounting on the microscope and
420 imaging.
421 A Nikon A1R-ER point-scanning confocal microscope was used to visualize the porosity of the
422 fluorescent fibrin matrix (Suppl. Figure 1A), Using Galvano scanning, image (1024 × 1024 pixel) stacks
423 were captured with 60× Apo (0.1 µm/pixel, NA 1.49l) objective with 0.25 µm spacing over 25 µm. The
424 LUNV laser was used at wavelength 633 nm and the pinhole size was 28.10 µm.
425
426 **Image Acquisition.** All other imaging was done on a Nikon Eclipse TE300 widefield epifluorescence
427 microscope (Nikon Instruments, Melville, NY) equipped with a NanoScanZ piezo Z stage insert (Prior
428 Scientific, Rockland, MA). See Table 1 for details of the imaging setup. Time-lapse video stacks were
429 collected with an iXON Life 888 EMCCD camera (Andor Technology, Belfast, Ireland) using NIS
430 Elements software v.5.11 (Nikon Instruments, Melville, NY). Fluorescently labeled parasites were
431 imaged using a pE-4000 LED illuminator (CoolLED, Andover England) and a 89402 Quad filter
432 (Chroma, Bellows Falls, VT). Stacks consisting of individual images (1024 pixel× 384 pixel) captured
433 0.5-1 µm apart in *z*, covering a total of 10-40 µm, were collected using either a 20× PlanApo λ (0.65
434 pixel/µm, NA 0.75) or 60 × PlanApo λ (0.22 pixel/µm, NA 1.4) objective as described in Table 1. The
435 same volume was successively imaged 60-360 times over the course of 64-302 seconds. The camera was
436 set to trigger mode, no binning, readout speed of 35 MHz, conversion gain of 3.8x, and EM gain setting
437 of 300.
438
439 **Table 1: Imaging parameters for the different experiments described**

Experiment	Objective	Fluorochrome (Excitation/emission wavelengths)	Image spacing in *z*	Exposure time per image	Number of Image stacks	Total time	Volume (*x, y, z*)

Microspheres (Matrigel)	60×	DragonGreen (490/507-530nm) tdTomato parasites (550/579-608 nm)	41 slices, 1µm apart	16 ms	60	64s	225.3 µm × 84.5 µm × 40 µm
Fibrin vs Matrigel and TgMIC2 KO directionality	20×	Hoechst 33342 (385/420-449 nm)	41 x 1 µm	16 ms	120	80s	665.6 µm × 249.6 µm × 40 µm
Force Mapping, WT (Fibrin)	60×	tdTomato parasites (550/579-608 nm) Fibrin (635/666-723 nm)	50 x 0.5 µm	16 ms	60	96s	225.3 µm × 84.5 µm × 24.5 µm
WT, TgMyoA KO, TgMIC2 KO; Brightfield (Matrigel, fibrin)	60×	N/A: Brightfield	21 x 1 µm	40 ms	360	302s	225.3 µm × 225.3 µm × 20 µm
Nuclear size vs constriction (Matrigel)	20×	Hoechst 33342 (385/420-449 nm) Anti-SAG1 Alexa 548 (550/579-608 nm)	41 x 1 µm	16 ms	60	80s	665.6 µm × 249.6 µm × 40 µm
TgMyoA KO Force Map (Fibrin)	60×	Hoechst 33342 (385/420-449 nm) Fibrin (635/666-723 nm)	50 x 0.5 µm	16 ms	60	96s	225.3 µm × 84.5 µm × 24.5 µm
TgMIC2 KO Force Map (Fibrin)	60×	YFP cytosol (490/507-530 nm) Fibrin (635/666-723 nm)	50 x 0.5 µm	16 ms	60	96s	225.3 µm × 84.5 µm × 24.5 µm

Tracking Parasite Motility. Datasets were analyzed in Imaris ×64 v. 9.2.0 (Bitplane AG, Zurich, Switzerland). Fluorescently labeled parasite nuclei were tracked using the ImarisTrack module within a 1018 pixel × 380 pixel region of interest to prevent artifacts from tracking objects near the border. Spot

detection used an estimated spot diameter of 3.0 × 3.0 × 6.0 µm (*x, y, z)*. A maximum distance of 6.0 µm and a maximum gap size of 2 frames were applied to the tracking algorithm. Tracks with durations under 10 seconds or displacements of less than 2 µm were discarded to avoid tracking artifacts and parasites moving by Brownian motion, respectively [13]. Accurate tracking was confirmed by visual inspection of parasite movements superimposed on their calculated trajectories.

For the comparison between Matrigel and fibrin, we analyzed three biological replicates, each consisting of three technical replicates. Student's T-tests were used to determine statistical significance between fibrin and Matrigel samples.

Fibrin Deformation with FIDVC. The Fast Iterative Digital Volume Correlation (FIDVC) algorithm was used to calculate 3D fibrin displacements [31] by comparing two consecutive image volumes. The image volumes were cropped to 384 × 384 pixels (*x,y)* × 48 slices (*z*) before running FIDVC. The initial interrogation window size was set to 32 × 32 × 32 and the program was run incrementally. The displacements arrows were plotted using a combination of previously described MATLAB code for 2D quiver color-coded for directionality [30] and custom MATLAB code. To filter out background signal, we calculated the mean magnitude of the 16,807 displacement vectors for each timepoint comparison in each dataset. The displacement detection threshold for that dataset was set as three standard deviations above the lowest of these mean values.

Rheology. A Lumicks C-Trap laser trap was used to determine the viscoelasticity of the fibrin. First, the power density spectrum (PDS) was calculated with 0.91 µm styrene beads in a flow cell. The beads were embedded in a fibrin gel, and a bead was captured in the laser trap. The flow cell was oscillated on the stage in the *y* dimension at different frequencies (1, 5, 10, 20, 50, 100 Hz), each for 5 seconds, at a fixed amplitude of 100 nm. The trap position and force in the *y* dimension were captured at 78 kHz. The elastic (in-phase) and viscous (out-of-phase) moduli were calculated using the bead's force trace. The data were analyzed in R studio. A sliding two-sided window filter, size 78, was applied to both traces. The position signal was fitted with the function $position = A * \sin(t * f - phase)$ using nonlinear least-squares with fit parameters for amplitude (A), frequency (f), and phase. The force readout was fit with the function $force = B * \sin(t * f - phase) + C * \cos(t * f - phase)$ using nonlinear least-squares with fitting parameters B and C, where B is the in-phase (elastic) component of the force. The C fit parameter divided by the velocity of the trap equals the viscous modulus.

478 **Figure legends**

479 **Figure 1: Parasites moving in 3D deform the surrounding Matrigel and undergo periodic**
480 **constrictions**. **(A)** In the linear motor model of motility, the TgMyoA motor (TgMyoA and its associated
481 light chains, TgMLC1 and either TgELC1 or TgELC2) is anchored to the parasite's inner membrane
482 complex (IMC) via TgGAP45 and the transmembrane proteins TgGAP40 and TgGAP50. The lumenal
483 portion of GAP50 is thought to interact with GAPM, a protein that spans the inner IMC membrane and
484 likely connects the entire glideosome to the underlying parasite cytoskeleton. Short actin filaments
485 located between the parasite plasma membrane and the IMC are connected to ligands on the substrate
486 through a linker protein, possibly GAC, which binds to the cytosolic tails of surface adhesins such as
487 TgMIC2. The TgMyoA motor displaces the actin filaments rearward; because the motor is connected to
488 the IMC and the actin is connected to the substrate, this causes the parasite to move forward relative to the
489 substrate. The vertical blue and red squiggles on TgGAP45 and TgMLC1 denote lipid anchors that attach
490 the proteins to the IMC [23, 28, 64]). Figure modified from [28] and re-used here under the terms of a
491 Creative Commons Attribution 4.0 International license (doi/10.1128/mSphere.00823-20). **(B)** Sequential
492 time series images in a single *z*-plane demonstrate that Dragon Green-labeled microspheres embedded
493 within the Matrigel are displaced towards moving tdTomato-expressing parasites; note displacement of
494 the green bead closest to the fixed crosshair in the merged images as the parasite moves from top left to
495 bottom right. See Video 1 for the entire time series, and Video 2 for a second example of bead
496 displacement by a moving parasite. **(C)** Brightfield images showing a constriction progressing from the
497 anterior to the posterior end of a parasite as the parasite moves forward one body length; see Video 3 for
498 entire time series. All wild-type parasites analyzed (n=99) formed at least one constriction per body
499 length of motility. Scale bars = 5 µm, timestamps in seconds.

500 **Figure 2: (A)** Confocal imaging of a 2.25 mg/ml fluorescent fibrin gel. A maximum fluorescence
501 intensity projection of 51 *z*-slices captured 0.25 µm apart is shown; scale bar = 10 µm. **(B)** Maximum
502 fluorescence intensity projections showing the trajectories of tdTomato-expressing wildtype parasites
503 moving in 3D in Matrigel (top) *vs.* fibrin (bottom). See Suppl. Figure 1 for quantitative comparison of the
504 motility parameters in the two matrices. Scale bar = 40 µm. **(C)** A parasite moving in a 1.3 mg/ml
505 fluorescent fibrin matrix (see Video 4) visibly deforms the matrix, as evident from the non-coincident
506 fluorescence signals in the highlighted area at the time points indicated (merge). Scale bar = 10 µm,
507 timestamps in seconds.

508 **Figure 3**: **Determining threshold of detection in 3D traction force mapping. (A)** A fluorescent fibrin
509 matrix containing wild-type parasites was imaged over 96 seconds (60 successive image volumes).
510 FIDVC was then used to calculate the 16,807 3D fibrin displacement vectors between successive pairs of

511 time points. The magnitudes of the 16,807 *x-y* displacement vectors are plotted for each of the 59 pairwise
512 timepoint comparisons. This dataset contained a single moving parasite, which moved intermittently
513 during the first part of the time course but not at the end, as indicated. For each time course, the two
514 consecutive timepoints that gave the lowest mean *x-y* displacement vector magnitude were used to set the
515 background threshold for that dataset: any displacements less than three standard deviations (3SD) above
516 this mean were considered background noise. **(B)** Expanded view of the 16,807 datapoints from the two
517 time point comparisons shown in purple and green in panel (A): no parasite movement was seen between
518 timepoints 6 and 7, while a single constricting parasite was seen moving between timepoints 7 and 8.
519 Arrow indicates the 3SD noise detection threshold; all points above this threshold are colored blue in
520 panels (A) and (B). **(C)** Displacement vectors with magnitudes greater than the 3SD threshold for the two
521 highlighted timepoint comparisons were mapped back onto the imaging volume; the cluster of
522 displacement vectors evident in the timepoints 7-8 comparison corresponds to the position of the single
523 moving parasite in the volume.

524 **<u>Figure 4</u>: 3D traction force mapping in fluorescent fibrin reveals that the matrix is periodically**
525 **pulled in towards the constriction during parasite motility**. **(A)** Sequential time series images in a
526 single *z*-plane of a tdTomato-expressing parasite moving in fibrin (boxed). Scale bar = 10 µm, timestamps
527 in seconds. **(B)** Force maps from the corresponding *z* subvolume plane of the data shown in (A); each
528 map depicts the motions of the fluorescent fibrin matrix between the two consecutive timepoints, as
529 indicated by the brackets. Arrow length (multiplied 24-fold for display) indicates the magnitude of matrix
530 displacement and arrow color the directionality (see color wheel). **(C)** Zoomed images showing the force
531 maps from the boxed region of panel B, after background subtraction (see text), overlaid on the parasite
532 images from panel A. Length of arrows indicating displacement magnitude are multiplied 15-fold for
533 display. Note inward displacement of the matrix in the second panel, outward displacement (relaxation) of
534 the matrix in the third panel, and no detectable displacement vectors in the fourth panel even though the
535 parasite continues to move. See Video 7 for real-time playback of the displacement vectors overlaid on
536 the moving parasite. **(D)** Zoomed overlays of the force maps (background subtracted) and images of a
537 moving parasite from a second dataset. The inwardly displaced matrix in this example did not relax back
538 to its original position within the time frame of the experiment. Arrow lengths indicating displacement
539 magnitude are multiplied 15-fold for display. See Video 8 for real-time playback of the displacement
540 vectors overlaid on the moving parasite. Scale bars in C and D = 5 µm. Empty red arrowheads indicate
541 position of the constriction.

542 **<u>Figure 5</u>: The constrictions are tightly linked with motility and are sufficiently narrow to deform**
543 **the parasite nucleus as it passes through. (A)** The time interval between constrictions during motility of

544 individual parasites (n=188 constrictions, 99 parasites). A negative time interval (black bars) corresponds
545 to the presence of two constrictions in the same parasite for the indicated amount of time. Green bars
546 denote back-to-back constrictions and grey bars denote a delay between constrictions for the indicated
547 amounts of time. For 27% of the constrictions (not plotted), no subsequent constriction occurred within
548 the time frame of the experiment. **(B)** Example of a parasite with two concurrent constrictions. Brightfield
549 images; scale bar = 5 µm; timestamps in seconds. **(C)** Number of constrictions observed *vs*. distance
550 traveled, expressed in terms of binned parasite body lengths (*i.e.*, multiples of 7 µm). **(D)** Width of non-
551 constricting parasites halfway along their longitudinal axis *vs.* width at the constriction halfway along the
552 parasite's longitudinal axis (n=19 constrictions, 15 parasites). **(E)** Dimensions of the nucleus (determined
553 by Hoechst 33342 staining) in non-constricting parasites *vs*. nuclei passing through a constriction (n=9
554 parasites, 21 constrictions). Nuclear length and width are defined as the diameters parallel and
555 perpendicular to the long axis of the parasite, respectively. Samples were compared by Student's two-
556 tailed t-test.

557 **<u>Figure 6</u>: 3D motility and force mapping of parasites lacking TgMyoA or TgMIC2. (A)** Brightfield
558 images showing TgMyoA knockout and TgMIC2 knockout parasites moving within a Matrigel matrix
559 without a detectable constriction. A wild-type parasite undergoing a typical constriction is shown for
560 comparison. The TgMyoA knockout parasite makes right-angled "stairstep" turn, and the TgMIC2
561 knockout parasite moves erratically in a tightly twisting arc. Scale bar = 5 µm, timestamps in seconds.
562 See Videos 11 and 12 for the entire time series for the TgMyoA and TgMIC2 knockout parasites. **(B-E)**
563 As in Figure 3A, the plots show the magnitudes of the 16,807 fibrin *x-y* displacement vectors between
564 each pair of successive image volumes generated in experiments using: (B) TgMyoA knockout parasites;
565 (C) TgMIC2 knockout parasites; (D) wild-type parasites; and (E) no added parasites (fibrin only). Periods
566 during the 96-second time course when parasites were moving are indicated. For each time course, the
567 two consecutive timepoints that gave the lowest mean displacement magnitude were used to set the
568 background threshold: any displacements less than three standard deviations (3SD) above this mean were
569 considered noise for that dataset. Examples of the force maps surrounding motile TgMyoA and TgMIC2
570 knockout parasites are shown in Suppl. Figures 7 and 8, respectively.
571

572 **Figure 7: Knockout of TgMIC2 results in the loss of the constriction and less directional motility.**
573 **(A)** Representative plots of nuclear shape (ratio of the nuclear diameters perpendicular *vs.* parallel to the
574 long axis of the parasite) in one wildtype and one TgMIC2 knockout parasite (black circles and green
575 squares, respectively), as the parasites moved over time. The wild-type parasite underwent multiple
576 concurrent constrictions along its trajectory. For the combined data from multiple parasites, see Suppl.
577 Figure 8D. **(B)** Ratio of parasite displacement (D) to trajectory length (L) for wildtype (n= 1399) and

578 TgMIC2 knockout (n= 165) parasites (black circles and green squares, respectively). The calculated
579 means (± SD) are from three independent biological replicates; see Suppl. Figure 8E. In panels (A) and
580 (B), "WT" refers to the TgMIC2 LoxP parasites [29] before treatment with rapamycin to excise *MIC2*.
581

582 **Supplemental figure legends**

583

584 **Suppl. Figure 1**: **Comparison of parasite motility in fluorescent fibrin *vs.* Matrigel. (A)** Comparison
585 of the maximum and mean speeds of parasites in 2.25 mg/ml fibrin *vs.* Matrigel. Horizontal bars indicate
586 mean (± SD) from 3 independent biological replicates (Matrigel n=853, Fibrin n=913). $p > 0.05$ for both
587 maximum and mean speed, Student's two-tailed t-test. **(B)** Comparison of the proportion of parasites
588 moving in 2.25 mg/ml fibrin *vs.* Matrigel. Horizontal bars indicate mean (± SD) from 3 independent
589 biological replicates (Matrigel n=853, Fibrin n=913). $p > 0.05$, Student's two-tailed t-test.

590 **Suppl. Figure 2:** **Rheological properties of the fibrin matrix.** The viscoelastic properties of the fibrin
591 matrix were measured by laser trapping of 0.91 µm styrene beads. **(A)** The laser trap position at 1 Hz (top
592 panel) and the resulting force as measured by the laser trap (bottom) show a primarily in-phase force
593 response. **(B)** The laser trap position and output force at 1-20Hz were used to calculate the elastic and
594 viscous properties of the matrix; these frequencies were chosen to encompass the approximate speed of a
595 moving parasite. Bars indicate mean (± SD).

596 **Suppl. Figure 3**: **All displacement vectors point in towards a moving parasite**. Matrix displacement
597 vectors from all subvolumes (49 (*x)* x 49 (*y*) X 7 (*z*)) in the image volume were calculated by FIDVC and
598 projected onto the *x-y, x-z* and *y-z* planes, as indicated (axis labels are in µm). Length of arrows indicate
599 displacement magnitude and are multiplied 10-fold for display. The data correspond to the parasite shown
600 in the second panel of Figure 4C and frame 2 of video 7. The moving parasite is outlined on each z slice
601 with red circles, and the position of the constriction is indicated by either an empty arrowhead (*x-y*) or a
602 black dot (*y-z*).

603 **Suppl. Figure 4**: **Pattern of pulling, holding and release of the matrix during individual constriction**
604 **events.** The number of consecutive frames in which: the matrix displaced in towards the parasite (pull);
605 no further matrix displacement was observed (hold); and the matrix moved away from the parasite
606 towards its original position (release) are indicated. n=9 parasites, 25 constrictions.

607 **Suppl. Figure 5**: **Additional examples showing that matrix displacement is directed primarily in**
608 **towards the constriction in moving parasites.** Empty red arrowheads indicate position of the

609 constriction and white arrows the direction of parasite travel. Length of black arrows indicating
610 displacement magnitude are multiplied 15-fold for display. Scale bars = 5 µm.

611 **Suppl. Figure 6**: **Fluorescent antibody against TgSAG1 is depleted from the parasite surface**
612 **anterior to the constriction and shed into the Matrigel matrix.** The top panels show the anti-TgSAG1
613 fluorescent signal; red empty arrowhead marks the location of the constriction. Middle panels show the
614 Hoechst 33342-stained nucleus, which stays in focus throughout the time series. Bottom panels show the
615 merged images (red = anti-TgSAG1, blue = Hoechst 33342). Scale bar = 5 µm; timestamps in seconds.
616 See Video 10 for the entire time series. All moving parasites examined (n=9) deposited trails containing
617 anti-SAG1 in the Matrigel.

618 **Suppl. Figure 7**: **The small number of TgMyoA knockout parasites that move more than one body**
619 **length produce no detectable force on the fibrin matrix. (A)** Sequential fluorescence images in a single
620 *z*-plane of a moving TgMyoA knockout parasite stained with Hoechst 33342 (to label the parasite
621 nucleus), **(B)** the corresponding force maps, and **(C)** the zoomed images showing the force maps from
622 panel B (boxed region), with background subtraction, overlaid on the parasite images from panel A. A red
623 crosshair placed at a fixed position in the images in panel (C) illustrates movement of the parasite. The
624 highlighted parasite continued to move for another 24 sec; no signal above background was seen on the
625 force maps at any time along its trajectory. Length of arrows indicating displacement magnitude are
626 multiplied 24-fold in (B) and 15-fold in (C) for display. Scale bar = 5 µm, timestamps in seconds.

627 **Suppl. Figure 8**: **TgMIC2 knockout parasites show no evidence of constrictions, produce no**
628 **detectable force on the fibrin matrix and move less directionally. (A)** Sequential fluorescence images
629 in a single *z*-plane of a moving TgMIC2 knockout parasite expressing YFP, **(B)** the corresponding force
630 maps, and **(C)** the zoomed images showing the force maps from panel B (boxed region), with background
631 subtraction, overlaid on the parasite images from panel A. A red crosshair placed at a fixed position in the
632 images in panel (C) illustrates movement of the parasite. The highlighted parasite continued to move for
633 another 18 sec; no signal above background was seen on the force maps at any time along its trajectory.
634 Length of arrows indicating displacement magnitude are multiplied 24-fold in (C) and 15-fold in (D) for
635 display. Scale bars = 10 µm (panel A), 5 µm (panel C); timestamps in seconds. **(D)** Ratio of nuclear
636 diameter perpendicular (width) *vs.* parallel (length) to the long axis of the parasite in moving wild-type
637 (WT; n=9) and TgMIC2 knockout (n=10) parasites, over time. For the wild-type parasites, triangles
638 indicate time points when the nucleus was passing through a constriction and circles when the nucleus
639 was not passing through a constriction. **(E)** Ratio of parasite displacement to trajectory length for wild-
640 type and TgMIC2 knockout parasites (three biological replicates, each consisting of three technical
641 replicates). The horizontal bars indicate means (+/- SD), which were compared by Student's two-sided t-

642 test. Note that in panels D and E, "WT" refers to the TgMIC2 LoxP parasites [29] before treatment with
643 rapamycin to excise *MIC2*.

644 **Suppl. Figure 9: Parasites move faster after the constriction has past the midway point on the**
645 **parasite's longitudinal axis.** The number of time points when the constriction was present either anterior
646 or posterior to the midway point along the parasite's longitudinal axis were determined. Only parasites
647 that progressed through one complete anterior-to-posterior constriction and neither stopped partway nor
648 initiated a second constriction while the original constriction was present were analyzed (n=20 parasites,
649 24 constrictions). It takes a constriction on average longer (*i.e.*, more timepoints) to progress from the
650 anterior tip of the parasite to the midway point along the parasite surface than it does from the midway
651 point to the posterior end. Bars indicate mean ± standard deviation; the data were compared by Student's
652 two-tailed t-test.

653

654 **Videos**

655

656 **Video 1:** Microsphere (green) being displaced towards a parasite (red) moving in Matrigel within in a
657 single *z* plane. Playback is in real time; scale bar = 5 µm. Single frames from this video are shown in
658 Figure 1B.
659 **Video 2:** Maximum intensity projection in *z* of microspheres (green) being displaced due to parasite (red)
660 movement within the Matrigel. Playback is in real time; scale bar = 5 µm.
661 **Video 3:** Brightfield imaging of a parasite undergoing a single constriction. Playback is in real time; scale
662 bar = 5 µm. Single frames from this video are shown in Figure 1C.
663 **Video 4:** Confocal fluorescence imaging of a 2.25 mg/ml fluorescent fibrin gel. 51 *x-y* slices captured
664 0.25 µm apart in *z* were reassembled into the volumetric view shown. Dimensions of the imaged volume
665 are shown at bottom left. See Figure 2A for maximum intensity projection of these data.
666 **Video 5:** Deformation of fluorescent fibrin (green) by a parasite (red; bottom) as it moves up through the
667 image stack. Playback is in real time; scale bar = 10 µm. Single frames from this video are shown in
668 Figure 2C.
669 **Video 6:** 3D displacement map surrounding the moving parasite shown in the second panel of Figure 4C
670 and frame 2 of Video 7. Length of arrows indicating displacement magnitude are multiplied 10-fold for
671 display. The parasite is outlined on each z plane with red circles. Single frames from this video displaying
672 projections onto the *x-y, x-z* and *y-z* planes are shown in Suppl. Figure 3.

673 **Video 7:** *x-y* displacement map overlaid on the moving parasite shown in Figure 4A-C. Playback is in real
674 time. Arrow size corresponds to relative displacement magnitude and arrow color to displacement
675 direction as described in Figure 4.
676 **Video 8:** *x-y* displacement map overlaid on the moving parasite shown in Figure 4D. Playback is in real
677 time. Arrow size corresponds to relative displacement magnitude and arrow color to displacement
678 direction as described in Figure 4.
679 **Video 9:** Brightfield imaging of a parasite undergoing two constrictions at the same time. Playback is in
680 real time; scale bar = 5 µm. Single frames from this video are shown in Figure 5B.
681 **Video 10:** Parasite labeled with Alexa546-conjugated anti-TgSAG1 (red) and Hoechst 33342 (blue)
682 undergoing a constriction. Playback is in real time; scale bar = 5 µm. Note the helical trail of shed
683 fluorescent antibody behind the moving parasite. Single frames from this video are shown in Suppl.
684 Figure 6.
685 **Video 11:** Brightfield imaging of a moving TgMyoA knockout parasite. Playback is in real time; scale
686 bar = 5 µm. Single frames from this video are shown in Figure 6A.
687 **Video 12:** Brightfield imaging of a moving TgMIC2 knockout parasite. Playback is in real time; scale bar
688 = 5 µm. Single frames from this video are shown in Figure 6A.
689

690 **Acknowledgements.** This work was supported by U.S. Public Health Service grants: AI139201 and
691 AI137767 (G.E.W): GM141743 and S10OD026884 for the Lumicks C-Trap (D.M.W); and T32AI055402
692 and F31AI145214 (R.V.S.), as well as American Heart Association grant 19PRE34370071 (R.V.S.) We
693 thank Nicole Bouffard and Dr. Douglas Taatjes of the UVM Larner College of Medicine Microscopy
694 Imaging Center (RRID# SCR_018821) for helpful advice and assistance with the Nikon A1R-ER
695 confocal microscope, which is supported by U.S. Public Health Service grant 1S10OD025030-01 from
696 the National Center for Research Resources. We thank: Dr. Markus Meissner for sharing the TgMyoA
697 and TgMIC2 knockout parasites; Dr. David Sibley for anti-TgSAG1 antibody; Drs. Mark Rould, Alex
698 Dunn, Christina Hueschen, Li-av Segev Zarko, John Boothroyd, Leanna Owen, Markus Meissner, and
699 Ulrich Schwarz for helpful discussions; Anne Snyder, Drs. Robyn Kent, Christina Hueschen, and Chris
700 Huston for helpful feedback on the manuscript. Finally, we thank Dr. Christian Franck for making the
701 FIDVC code used in this work freely available through GitHub.
702

703 **References**

704 1. World malaria report. Geneva: World Health Organization, 2021.

705 2. Sow SO, Muhsen K, Nasrin D, Blackwelder WC, Wu Y, Farag TH, et al. The Burden of
706 Cryptosporidium Diarrheal Disease among Children < 24 Months of Age in Moderate/High Mortality

Regions of Sub-Saharan Africa and South Asia, Utilizing Data from the Global Enteric Multicenter Study (GEMS). PLoS Negl Trop Dis. 2016;10(5):e0004729. Epub 2016/05/25. doi: 10.1371/journal.pntd.0004729. PubMed PMID: 27219054; PubMed Central PMCID: PMCPMC4878811

3. Bigna JJ, Tochie JN, Tounouga DN, Bekolo AO, Ymele NS, Youda EL, et al. Global, regional, and country seroprevalence of Toxoplasma gondii in pregnant women: a systematic review, modelling and meta-analysis. Sci Rep. 2020;10(1):12102. Epub 2020/07/23. doi: 10.1038/s41598-020-69078-9. PubMed PMID: 32694844; PubMed Central PMCID: PMCPMC7374101.

4. Flegr J, Prandota J, Sovičková M, Israili ZH. Toxoplasmosis--a global threat. Correlation of latent toxoplasmosis with specific disease burden in a set of 88 countries. PloS one. 2014;9(3):e90203. Epub 2014/03/26. doi: 10.1371/journal.pone.0090203. PubMed PMID: 24662942; PubMed Central PMCID: PMCPMC3963851.

5. Pappas G, Roussos N, Falagas ME. Toxoplasmosis snapshots: global status of *Toxoplasma gondii* seroprevalence and implications for pregnancy and congenital toxoplasmosis. International journal for parasitology. 2009;39(12):1385-94. Epub 2009/05/13. doi: 10.1016/j.ijpara.2009.04.003. PubMed PMID: 19433092.

6. Rothova A. Ocular involvement in toxoplasmosis. British Journal of Ophthalmology. 1993;77(6):371-7. doi: doi: 10.1136/bjo.77.6.371.

7. Su E, Honda A, Latkany P. Ocular Disease due to *Toxoplasma gondii*. In: Weiss LM, Kim K, editors. *Toxoplasma gondii* - The Model Apicomplexan: Perspectives and Methods. Second ed. London, UK: Academic Press; 2014. p. 161-92.

8. Daher W, Plattner F, Carlier MF, Soldati-Favre D. Concerted action of two formins in gliding motility and host cell invasion by *Toxoplasma gondii*. PLoS Pathog. 2010;6(10). PubMed PMID: 20949068.

9. Elsheikha HM, Marra CM, Zhu XQ. Epidemiology, Pathophysiology, Diagnosis, and Management of Cerebral Toxoplasmosis. Clin Microbiol Rev. 2021;34(1). Epub 2020/11/27. doi: 10.1128/cmr.00115-19. PubMed PMID: 33239310.

10. Barragan A, Brossier F, Sibley LD. Transepithelial migration of *Toxoplasma gondii* involves an interaction of intercellular adhesion molecule 1 (ICAM-1) with the parasite adhesin MIC2. Cell Microbiol. 2005;7(4):561-8. PubMed PMID: 15760456.

11. Harker KS, Ueno N, Lodoen MB. *Toxoplasma gondii* Dissemination: A Parasite's Journey through the Infected Host. Parasite immunology. 2015;37:141-9. Epub 2014/11/20. doi: 10.1111/pim.12163. PubMed PMID: 25408224.

12. Meissner M, Schluter D, Soldati D. Role of *Toxoplasma gondii* myosin A in powering parasite gliding and host cell invasion. Science. 2002;298(5594):837-40. PubMed PMID: 12399593.

13. Leung JM, Rould MA, Konradt C, Hunter CA, Ward GE. Disruption of *TgPHIL1* alters specific parameters of *Toxoplasma gondii* motility measured in a quantitative, three-dimensional live motility assay. PloS one. 2014;9(1):e85763. Epub 2014/02/04. doi: 10.1371/journal.pone.0085763. PubMed PMID: 24489670; PubMed Central PMCID: PMC3906025.

14. Frenal K, Dubremetz JF, Lebrun M, Soldati-Favre D. Gliding motility powers invasion and egress in Apicomplexa. Nat Rev Microbiol. 2017;15(11):645-60. doi: 10.1038/nrmicro.2017.86. PubMed PMID: 28867819.

748 15. Heintzelman MB. Gliding motility in apicomplexan parasites. Seminars in cell & developmental
749 biology. 2015. Epub 2015/10/03. doi: 10.1016/j.semcdb.2015.09.020. PubMed PMID: 26428297.

750 16. Jacot D, Tosetti N, Pires I, Stock J, Graindorge A, Hung YF, et al. An Apicomplexan Actin-Binding
751 Protein Serves as a Connector and Lipid Sensor to Coordinate Motility and Invasion. Cell Host
752 Microbe. 2016;20(6):731-43. doi: 10.1016/j.chom.2016.10.020. PubMed PMID: 27978434.

753 17. Sibley LD. Intracellular parasite invasion strategies. Science. 2004;304(5668):248-53. PubMed
754 PMID: 15073368.

755 18. Kappe S, Bruderer T, Gantt S, Fujioka H, Nussenzweig V, Ménard R. Conservation of a gliding
756 motility and cell invasion machinery in Apicomplexan parasites. J Cell Biol. 1999;147(5):937-44.
757 Epub 1999/12/01. doi: 10.1083/jcb.147.5.937. PubMed PMID: 10579715; PubMed Central PMCID:
758 PMCPMC2169348.

759 19. Andenmatten N, Egarter S, Jackson AJ, Jullien N, Herman JP, Meissner M. Conditional genome
760 engineering in *Toxoplasma gondii* uncovers alternative invasion mechanisms. Nature methods.
761 2012;10(2):125-7. Epub 2012/12/25. doi: 10.1038/nmeth.2301. PubMed PMID: 23263690; PubMed
762 Central PMCID: PMC3605914.

763 20. Egarter S, Andenmatten N, Jackson AJ, Whitelaw JA, Pall G, Black JA, et al. The *Toxoplasma* Acto-
764 MyoA motor complex is important but not essential for gliding motility and host cell invasion. PloS
765 one. 2014;9(3):e91819. Epub 2014/03/19. doi: 10.1371/journal.pone.0091819. PubMed PMID:
766 24632839; PubMed Central PMCID: PMC3954763.

767 21. Tosetti N, Dos Santos Pacheco N, Soldati-Favre D, Jacot D. Three F-actin assembly centers regulate
768 organelle inheritance, cell-cell communication and motility in Toxoplasma gondii. eLife. 2019;8.
769 Epub 2019/02/13. doi: 10.7554/eLife.42669. PubMed PMID: 30753127; PubMed Central PMCID:
770 PMCPMC6372287.

771 22. Dobrowolski JM, Sibley LD. *Toxoplasma* invasion of mammalian cells is powered by the actin
772 cytoskeleton of the parasite. Cell. 1996;84(6):933-9.

773 23. Frenal K, Polonais V, Marq JB, Stratmann R, Limenitakis J, Soldati-Favre D. Functional dissection
774 of the apicomplexan glideosome molecular architecture. Cell Host Microbe. 2010;8(4):343-57.
775 PubMed PMID: 20951968.

776 24. Gras S, Jimenez-Ruiz E, Klinger CM, Schneider K, Klingl A, Lemgruber L, et al. An endocytic-
777 secretory cycle participates in Toxoplasma gondii in motility. PLoS Biol. 2019;17(6):e3000060. Epub
778 2019/06/25. doi: 10.1371/journal.pbio.3000060. PubMed PMID: 31233488.

779 25. Meissner M, Ferguson DJ, Frischknecht F. Invasion factors of apicomplexan parasites: essential or
780 redundant? Current opinion in microbiology. 2013;16(4):438-44. Epub 2013/06/04. doi:
781 10.1016/j.mib.2013.05.002. PubMed PMID: 23727286.

782 26. Tardieux I, Baum J. Reassessing the mechanics of parasite motility and host-cell invasion. J Cell Biol.
783 2016;214(5):507-15. doi: 10.1083/jcb.201605100. PubMed PMID: 27573462; PubMed Central
784 PMCID: PMCPMC5004448.

785 27. Whitelaw JA, Latorre-Barragan F, Gras S, Pall GS, Leung JM, Heaslip A, et al. Surface attachment,
786 promoted by the actomyosin system of *Toxoplasma gondii* is important for efficient gliding motility
787 and invasion. BMC Biol. 2017;15(1):1. doi: 10.1186/s12915-016-0343-5. PubMed PMID: 28100223;
788 PubMed Central PMCID: PMCPMC5242020.

789 28. Rompikuntal PK, Kent RS, Foe IT, Deng B, Bogyo M, Ward GE. Blocking Palmitoylation of
790 Toxoplasma gondii Myosin Light Chain 1 Disrupts Glideosome Composition but Has Little Impact
791 on Parasite Motility. mSphere. 2021;6(3). Epub 2021/05/21. doi: 10.1128/mSphere.00823-20.
792 PubMed PMID: 34011689.

793 29. Gras S, Jackson A, Woods S, Pall G, Whitelaw J, Leung JM, et al. Parasites lacking the micronemal
794 protein MIC2 are deficient in surface attachment and host cell egress, but remain virulent *in vivo*
795 [version 1]. Wellcome Open Research. 2017;2:32. doi: 10.12688/wellcomeopenres.11594.1.

796 30. Owen LM, Adhikari AS, Patel M, Grimmer P, Leijnse N, Kim MC, et al. A cytoskeletal clutch
797 mediates cellular force transmission in a soft, three-dimensional extracellular matrix. Mol Biol Cell.
798 2017;28(14):1959-74. Epub 2017/06/09. doi: 10.1091/mbc.E17-02-0102. PubMed PMID: 28592635;
799 PubMed Central PMCID: PMCPMC5541846.

800 31. Bar-Kochba E, Toyjanova J, Andrews E, Kim K-S, Franck C. A Fast Iterative Digital Volume
801 Correlation Algorithm for Large Deformations. Experimental Mechanics2015. p. 261-74.

802 32. Huynh MH, Carruthers VB. *Toxoplasma* MIC2 is a major determinant of invasion and virulence. PLoS
803 Pathog. 2006;2(8):e84. PubMed PMID: 16933991.

804 33. Munter S, Sabass B, Selhuber-Unkel C, Kudryashev M, Hegge S, Engel U, et al. *Plasmodium*
805 sporozoite motility is modulated by the turnover of discrete adhesion sites. Cell Host Microbe.
806 2009;6(6):551-62. PubMed PMID: 20006843.

807 34. Hakansson S, Morisaki H, Heuser J, Sibley LD. Time-lapse video microscopy of gliding motility in
808 *Toxoplasma gondii* reveals a novel, biphasic mechanism of cell locomotion. Mol Biol Cell.
809 1999;10(11):3539-47.

810 35. Pavlou G, Touquet B, Vigetti L, Renesto P, Bougdour A, Debarre D, et al. Coupling Polar Adhesion
811 with Traction, Spring and Torque Forces Allows High Speed Helical Migration of the Protozoan
812 Parasite Toxoplasma. ACS Nano. 2020;14:7121-39. Epub 2020/05/21. doi:
813 10.1021/acsnano.0c01893. PubMed PMID: 32432851.

814 36. Munera Lopez J, Tengganu IF, Liu J, Murray JM, Arias Padilla LF, Zhang Y, et al. An apical protein,
815 Pcr2, is required for persistent movement by the human parasite Toxoplasma gondii. PLoS Pathog.
816 2022;18(8):e1010776. Epub 2022/08/23. doi: 10.1371/journal.ppat.1010776. PubMed PMID:
817 35994509; PubMed Central PMCID: PMCPMC9436145.

818 37. Freyvogel TA. Shape, movement in situ and locomotion of plasmodial ookinetes. Acta Trop.
819 1966;23(3):201-22. Epub 1966/01/01. PubMed PMID: 4380662.

820 38. Vlachou D, Zimmermann T, Cantera R, Janse CJ, Waters AP, Kafatos FC. Real-time, in vivo analysis
821 of malaria ookinete locomotion and mosquito midgut invasion. Cell Microbiol. 2004;6(7):671-85.
822 Epub 2004/06/10. doi: 10.1111/j.1462-5822.2004.00394.x. PubMed PMID: 15186403.

823 39. Zieler H, Dvorak JA. Invasion in vitro of mosquito midgut cells by the malaria parasite proceeds by a
824 conserved mechanism and results in death of the invaded midgut cells. Proceedings of the National
825 Academy of Sciences of the United States of America. 2000;97(21):11516-21. Epub 2000/10/12. doi:
826 10.1073/pnas.97.21.11516. PubMed PMID: 11027351; PubMed Central PMCID: PMCPMC17232.

827 40. Alexander DL, Mital J, Ward GE, Bradley P, Boothroyd JC. Identification of the moving junction
828 complex of *Toxoplasma gondii*: a collaboration between distinct secretory organelles. PLoS Pathog.
829 2005;1(2):e17. doi: 10.1371/journal.ppat.0010017. PubMed PMID: 16244709.

41. Besteiro S, Dubremetz JF, Lebrun M. The moving junction of apicomplexan parasites: a key structure for invasion. Cell Microbiol. 2011;13(6):797-805. PubMed PMID: 21535344.

42. Dubremetz JF. Host cell invasion by *Toxoplasma gondii* [see comments]. Trends Microbiol. 1998;6(1):27-30.

43. Lebrun M, Michelin A, El Hajj H, Poncet J, Bradley PJ, Vial H, et al. The rhoptry neck protein RON4 re-localizes at the moving junction during *Toxoplasma gondii* invasion. Cell Microbiol. 2005;7(12):1823-33. PubMed PMID: 16309467.

44. Porchet-Hennere E, Torpier, G. [Relationships between *Toxoplasma* and its host cell]. Protistologica. 1983;19:357-70.

45. Aikawa M, Miller LH, Johnson J, Rabbege J. Erythrocyte entry by malarial parasites. A moving junction between erythrocyte and parasite. J Cell Biol. 1978;77(1):72-82.

46. Bargieri DY, Andenmatten N, Lagal V, Thiberge S, Whitelaw JA, Tardieux I, et al. Apical membrane antigen 1 mediates apicomplexan parasite attachment but is dispensable for host cell invasion. Nature communications. 2013;4:2552. Epub 2013/10/11. doi: 10.1038/ncomms3552. PubMed PMID: 24108241.

47. Mital J, Meissner M, Soldati D, Ward GE. Conditional expression of *Toxoplasma gondii* apical membrane antigen-1 (TgAMA1) demonstrates that TgAMA1 plays a critical role in host cell invasion. Mol Biol Cell. 2005;16(9):4341-9. doi: 10.1091/mbc.E05-04-0281. PubMed PMID: 16000372.

48. Pavlou G, Biesaga M, Touquet B, Lagal V, Balland M, Dufour A, et al. Toxoplasma Parasite Twisting Motion Mechanically Induces Host Cell Membrane Fission to Complete Invasion within a Protective Vacuole. Cell Host Microbe. 2018;24(1):81-96.e5. Epub 2018/07/17. doi: 10.1016/j.chom.2018.06.003. PubMed PMID: 30008293.

49. Hueschen CL, Zarko L-aS, Chen J-H, LeGros MA, Larabell CA, Boothroyd JC, et al. Emergent Actin Flows Explain Diverse Parasite Gliding Modes. bioRxiv. 2022:2022.06.08.495399. doi: 10.1101/2022.06.08.495399.

50. Dubremetz JF, Rodriguez C, Ferreira E. *Toxoplasma gondii*: redistribution of monoclonal antibodies on tachyzoites during host cell invasion. Exp Parasitol. 1985;59(1):24-32.

51. Herm-Gotz A, Weiss S, Stratmann R, Fujita-Becker S, Ruff C, Meyhofer E, et al. *Toxoplasma gondii* myosin A and its light chain: a fast, single-headed, plus-end-directed motor. EMBO J. 2002;21(9):2149-58.

52. Mordue DG, Desai N, Dustin M, Sibley LD. Invasion by *Toxoplasma gondii* Establishes a Moving Junction That Selectively Excludes Host Cell Plasma Membrane Proteins on the Basis of Their Membrane Anchoring. J Exp Med. 1999;190(12):1783-92.

53. Quadt KA, Streichfuss M, Moreau CA, Spatz JP, Frischknecht F. Coupling of Retrograde Flow to Force Production During Malaria Parasite Migration. ACS Nano. 2016;10(2):2091-102. Epub 2016/01/23. doi: 10.1021/acsnano.5b06417. PubMed PMID: 26792112.

54. Stadler RV, Nelson SR, Warshaw DM, Ward GE. A circular zone of attachment to the extracellular matrix acts as a guidance system for Toxoplasma gondii 3D motility. bioRxiv. 2022:2022.06.08.495400. doi: 10.1101/2022.06.08.495400.

869 55. Frenal K, Soldati-Favre D. Plasticity and Redundancy in Proteins Important for *Toxoplasma* Invasion.
870 PLoS Pathog. 2015;11(8):e1005069. Epub 2015/08/14. doi: 10.1371/journal.ppat.1005069. PubMed
871 PMID: 26270966; PubMed Central PMCID: PMC4536160.

872 56. Lamarque MH, Roques M, Kong-Hap M, Tonkin ML, Rugarabamu G, Marq JB, et al. Plasticity and
873 redundancy among AMA-RON pairs ensure host cell entry of *Toxoplasma* parasites. Nature
874 communications. 2014;5:4098. Epub 2014/06/18. doi: 10.1038/ncomms5098. PubMed PMID:
875 24934579.

876 57. Lammermann T, Bader BL, Monkley SJ, Worbs T, Wedlich-Soldner R, Hirsch K, et al. Rapid
877 leukocyte migration by integrin-independent flowing and squeezing. Nature. 2008;453(7191):51-5.
878 doi: 10.1038/nature06887. PubMed PMID: 18451854.

879 58. Berg HC, Turner L. Movement of microorganisms in viscous environments. Nature.
880 1979;278(5702):349-51. Epub 1979/03/22. doi: 10.1038/278349a0. PubMed PMID: 370610.

881 59. Ferrero RL, Lee A. Motility of Campylobacter jejuni in a viscous environment: comparison with
882 conventional rod-shaped bacteria. J Gen Microbiol. 1988;134(1):53-9. Epub 1988/01/01. doi:
883 10.1099/00221287-134-1-53. PubMed PMID: 3053972.

884 60. Hazell SL, Lee A, Brady L, Hennessy W. Campylobacter pyloridis and gastritis: association with
885 intercellular spaces and adaptation to an environment of mucus as important factors in colonization of
886 the gastric epithelium. J Infect Dis. 1986;153(4):658-63. Epub 1986/04/01. doi:
887 10.1093/infdis/153.4.658. PubMed PMID: 3950447.

888 61. Kaiser GE, Doetsch RN. Letter: Enhanced translational motion of Leptospira in viscous environments.
889 Nature. 1975;255(5510):656-7. Epub 1975/06/19. doi: 10.1038/255656a0. PubMed PMID: 1134561.

890 62. Kimsey RB, Spielman A. Motility of Lyme disease spirochetes in fluids as viscous as the extracellular
891 matrix. J Infect Dis. 1990;162(5):1205-8. Epub 1990/11/01. doi: 10.1093/infdis/162.5.1205. PubMed
892 PMID: 2230247.

893 63. Roos DS, Donald RG, Morrissette NS, Moulton AL. Molecular tools for genetic dissection of the
894 protozoan parasite *Toxoplasma gondii*. Methods in Cell Biology. 451994. p. 27-63.

895 64. Foe IT, Child MA, Majmudar JD, Krishnamurthy S, van der Linden WA, Ward GE, et al. Global
896 Analysis of Palmitoylated Proteins in *Toxoplasma gondii*. Cell Host Microbe. 2015;18(4):501-11.
897 Epub 2015/10/16. doi: 10.1016/j.chom.2015.09.006. PubMed PMID: 26468752.

898

Figure 1

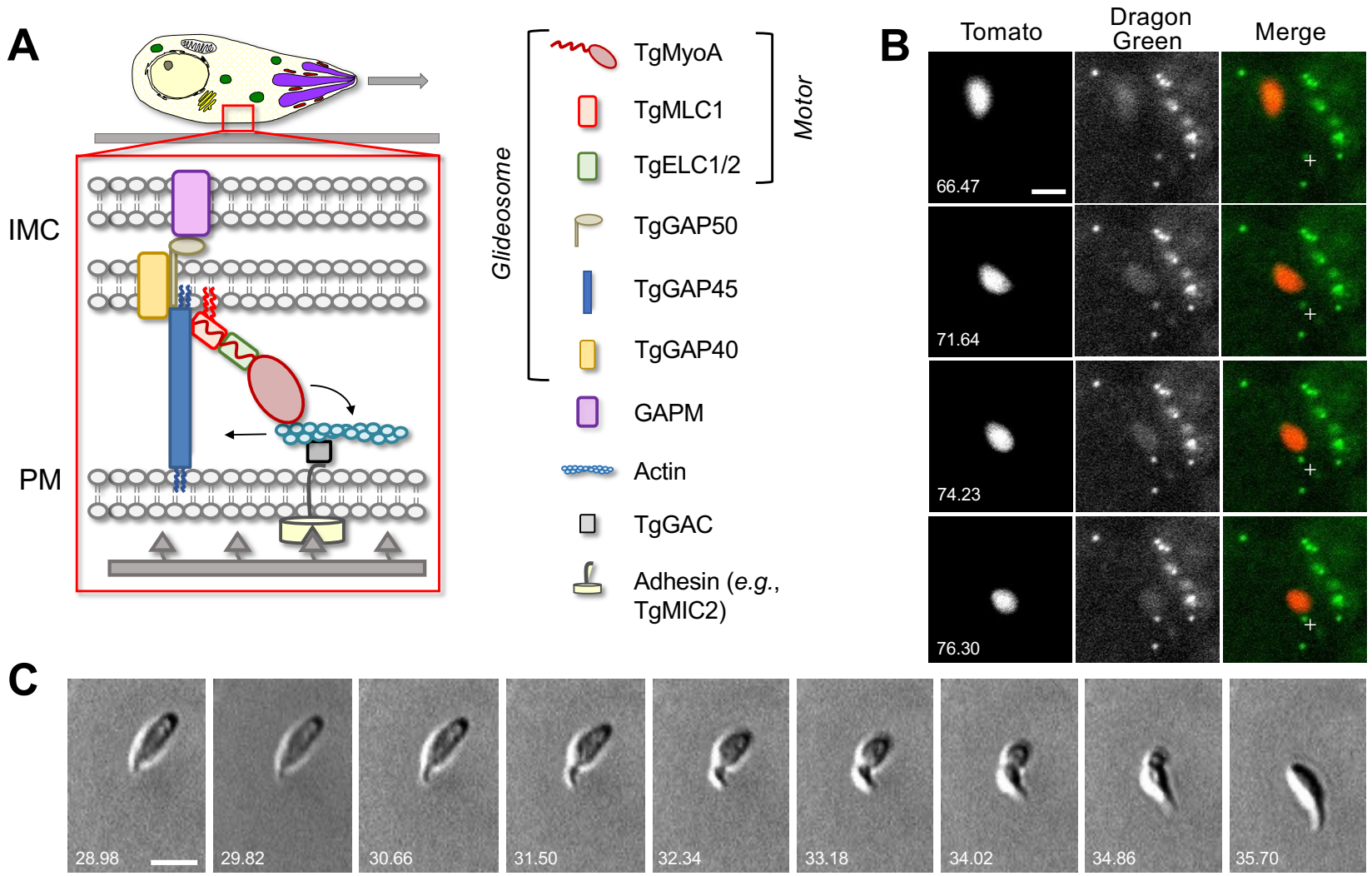
A
IMC
PM
Glideosome
Motor
TgMyoA
TgMLC1
TgELC1/2
TgGAP50
TgGAP45
TgGAP40
GAPM
Actin
TgGAC
Adhesin (e.g., TgMIC2)
B
Tomato
Dragon Green
Merge
66.47
71.64
74.23
76.30
C
28.98
29.82
30.66
31.50
32.34
33.18
34.02
34.86
35.70

Figure 2

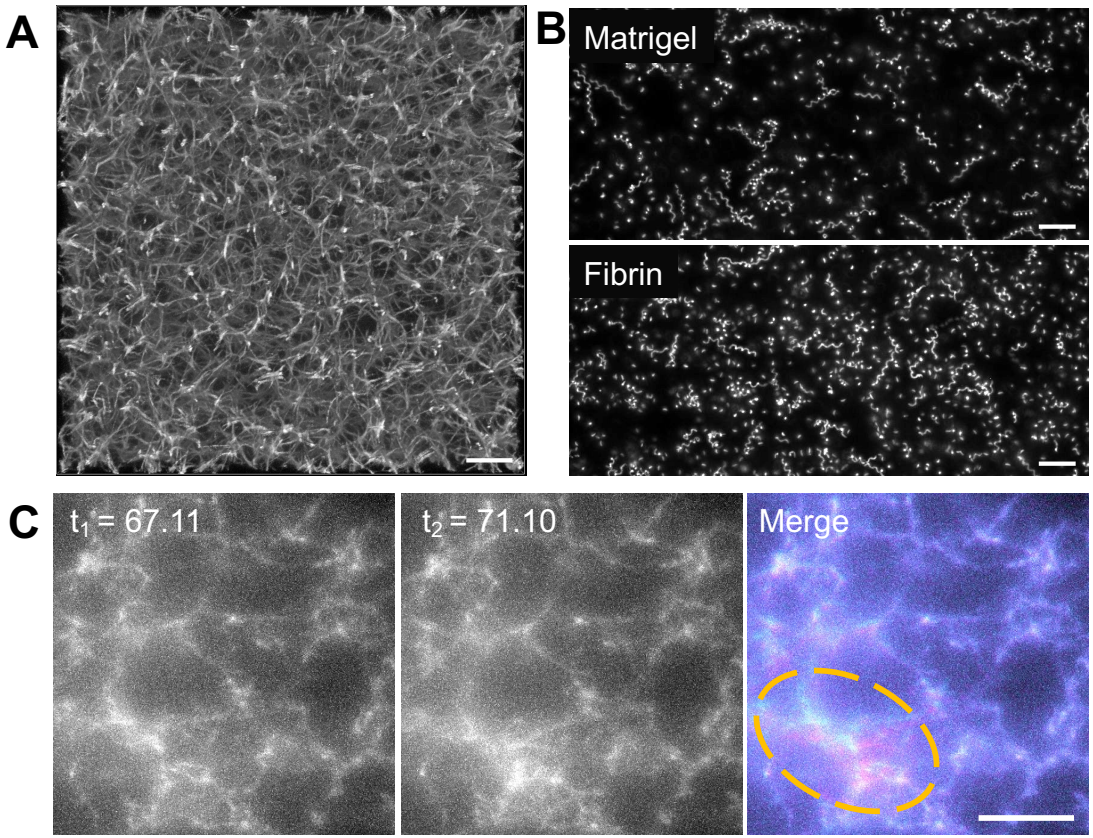

Figure 3

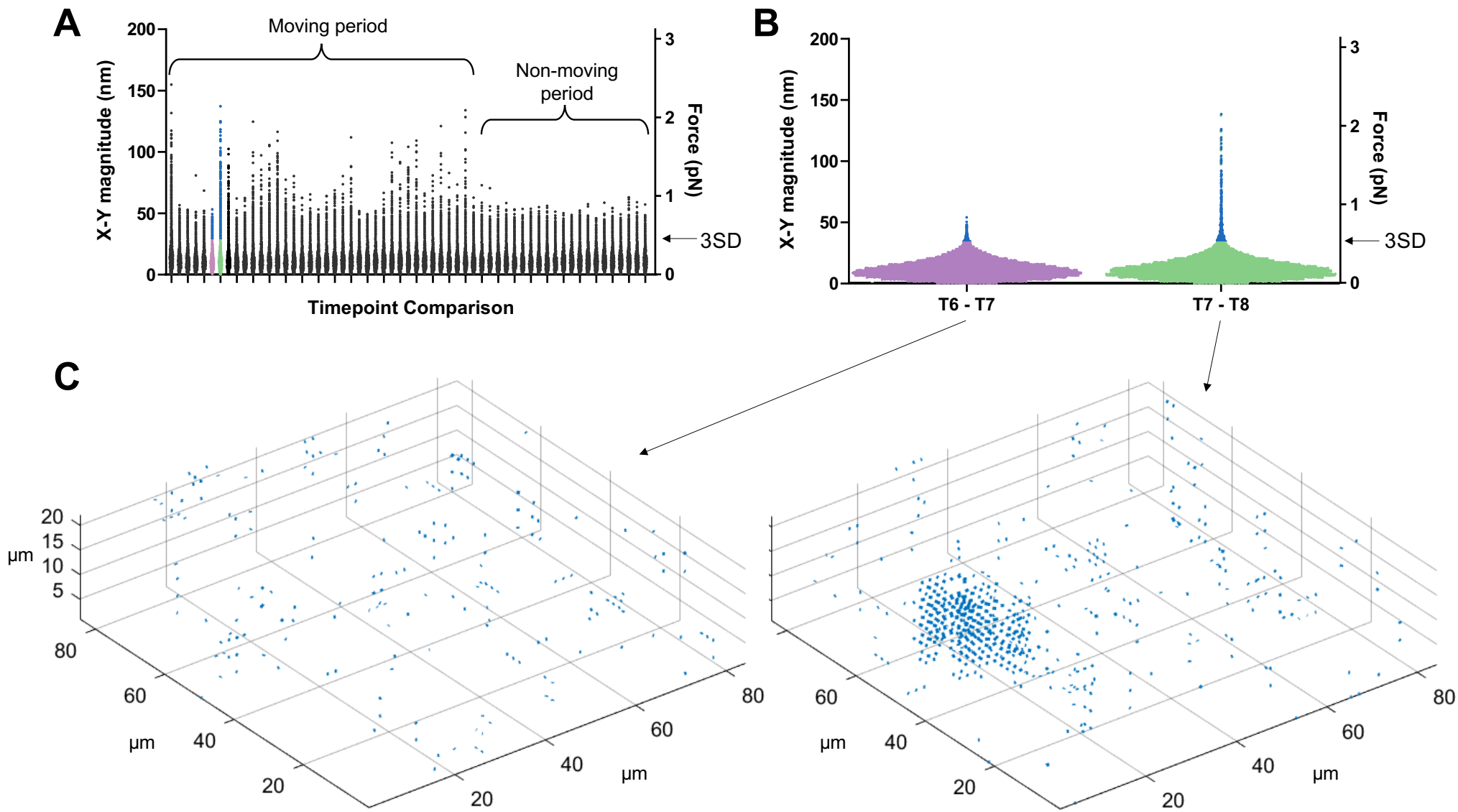
A
Moving period
Non-moving period
X-Y magnitude (nm)
Force (pN)
3SD
Timepoint Comparison
B
X-Y magnitude (nm)
Force (pN)
3SD
T6 - T7
T7 - T8
C
µm
µm
µm
µm

Figure 4

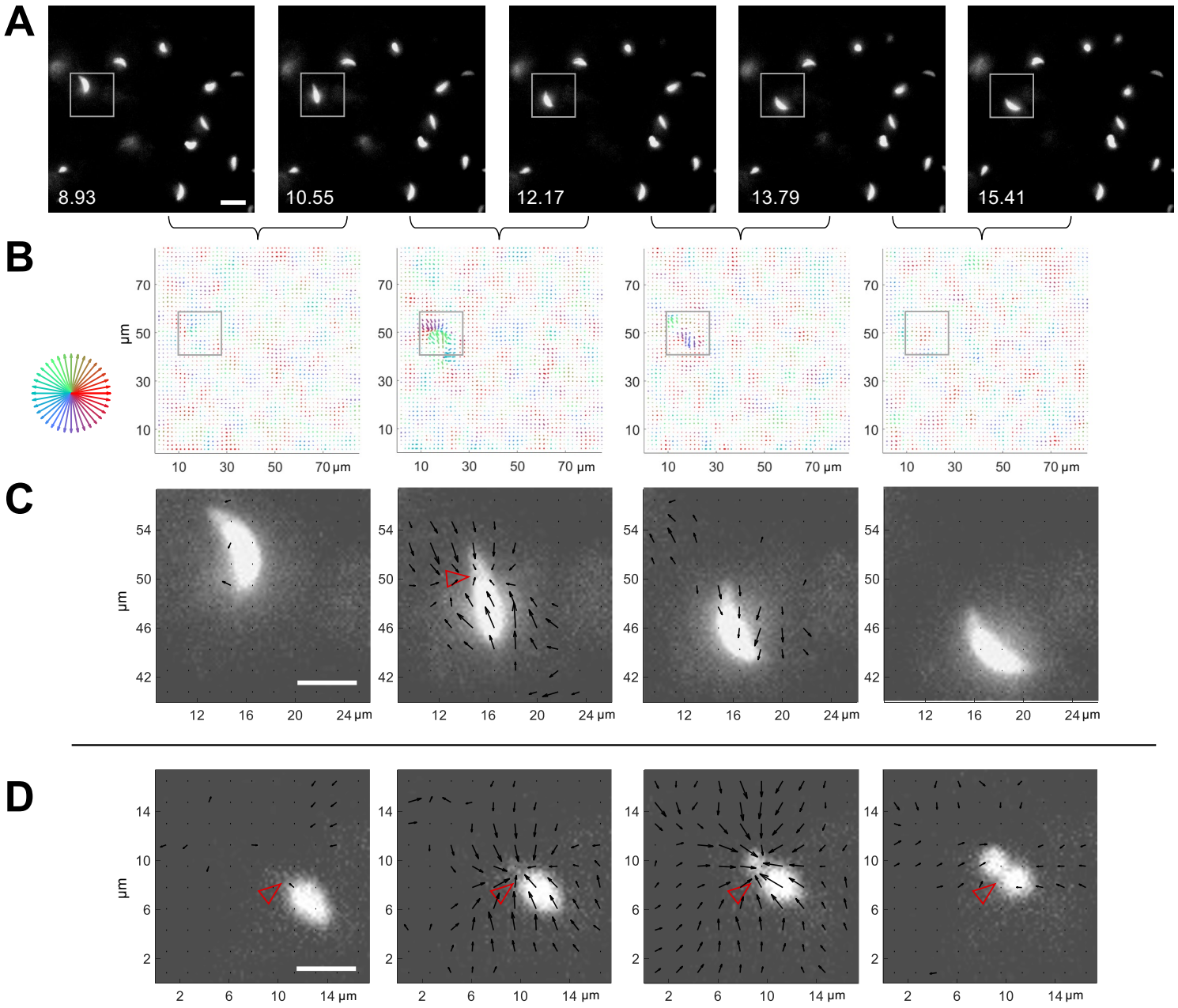

Figure 5

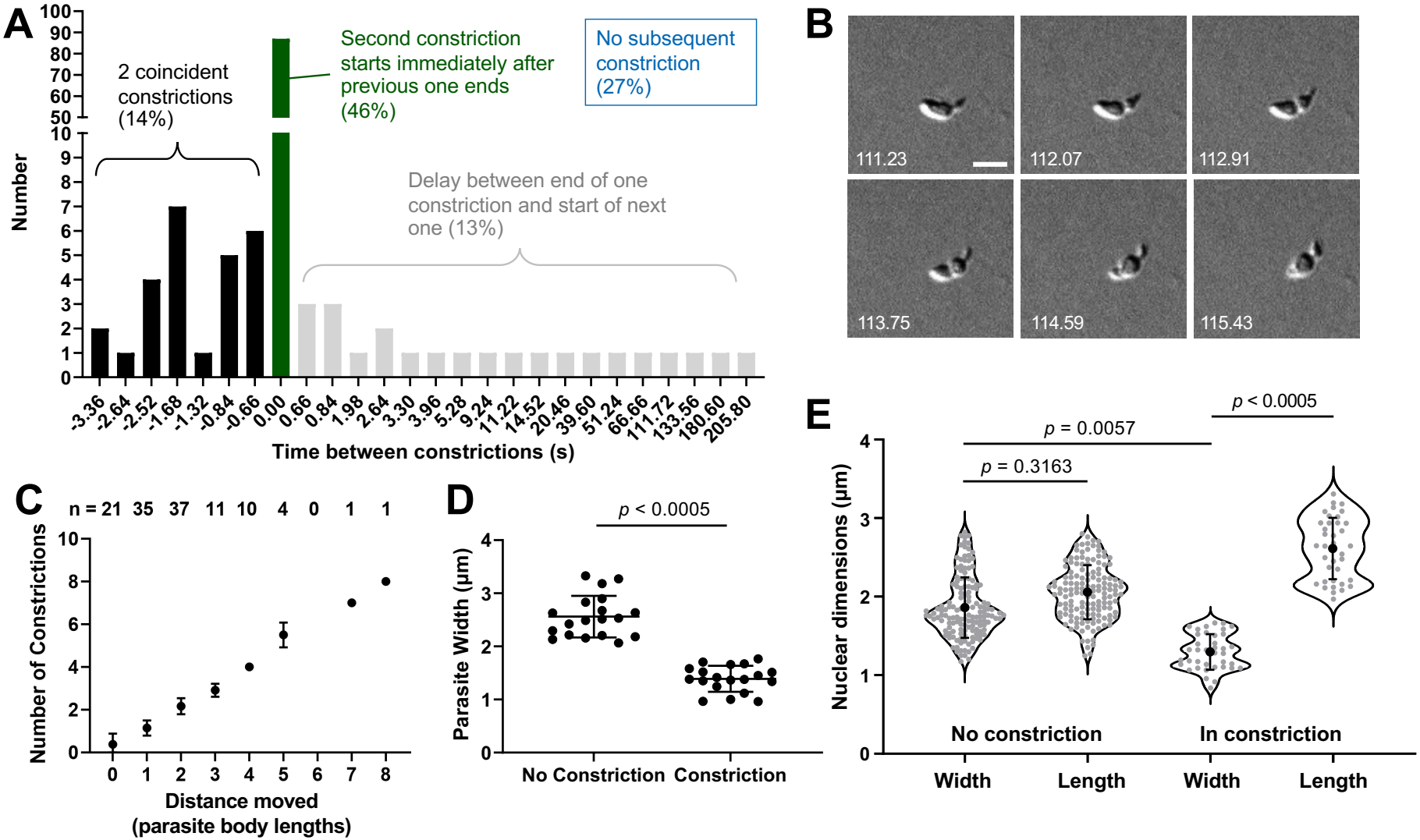
A
Number
2 coincident constrictions (14%)
Second constriction starts immediately after previous one ends (46%)
No subsequent constriction (27%)
Delay between end of one constriction and start of next one (13%)
-3.36 -2.64 -2.52 -1.68 -1.32 -0.84 -0.66 0.00 0.66 0.84 1.98 2.64 3.30 3.96 5.28 9.24 11.22 14.52 20.46 39.60 51.24 66.66 111.72 133.56 180.60 205.80
Time between constrictions (s)
B
111.23
112.07
112.91
113.75
114.59
115.43
C
n = 21 35 37 11 10 4 0 1 1
Number of Constrictions
Distance moved (parasite body lengths)
D
p < 0.0005
Parasite Width (µm)
No Constriction
Constriction
E
p = 0.0057
p < 0.0005
p = 0.3163
Nuclear dimensions (µm)
No constriction
In constriction
Width
Length
Width
Length

Figure 6

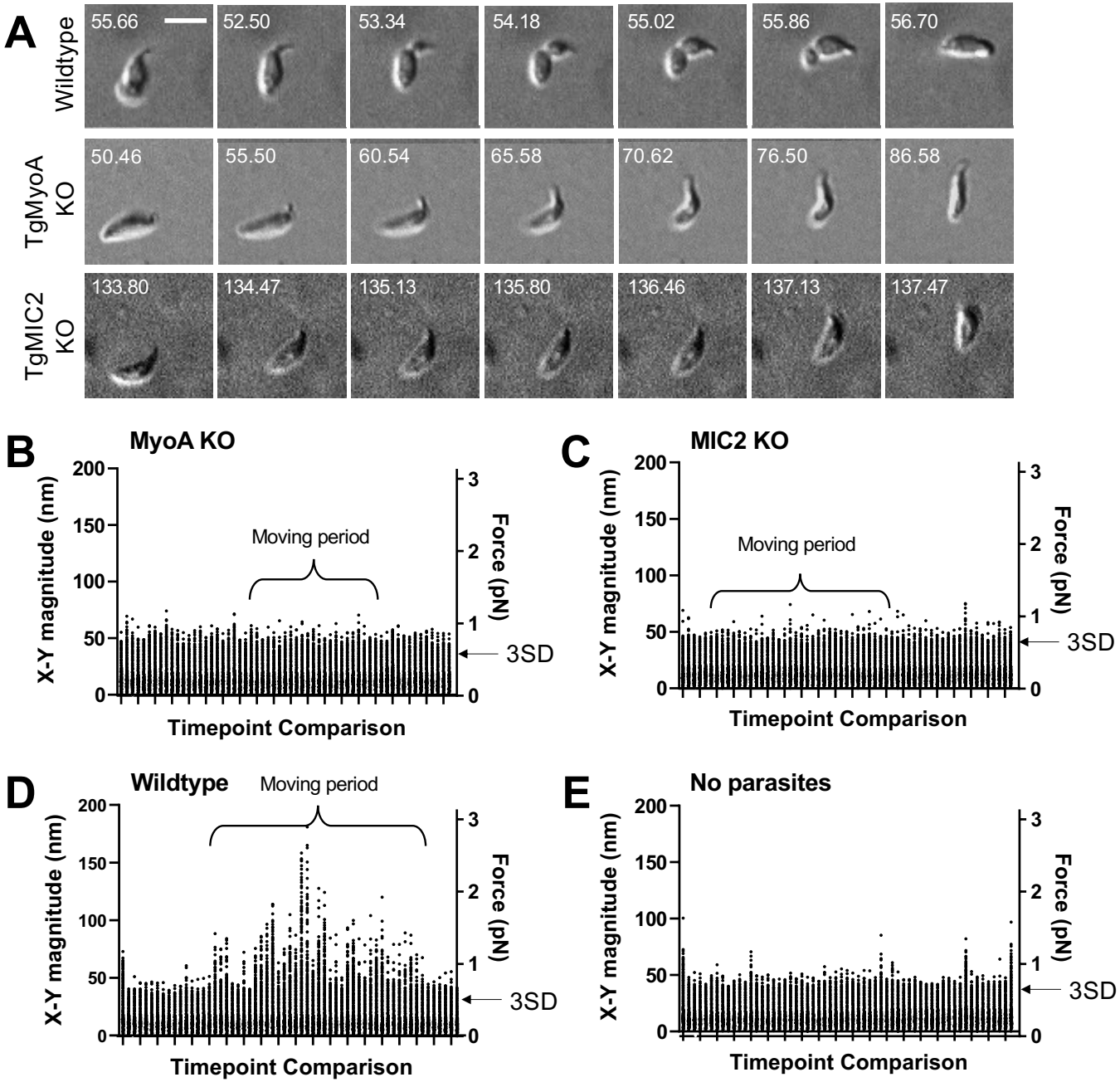
A
Wildtype
55.66
52.50
53.34
54.18
55.02
55.86
56.70
TgMyoA KO
50.46
55.50
60.54
65.58
70.62
76.50
86.58
TgMIC2 KO
133.80
134.47
135.13
135.80
136.46
137.13
137.47
B
MyoA KO
Moving period
X-Y magnitude (nm)
Force (pN)
3SD
Timepoint Comparison
C
MIC2 KO
Moving period
X-Y magnitude (nm)
Force (pN)
3SD
Timepoint Comparison
D
Wildtype
Moving period
X-Y magnitude (nm)
Force (pN)
3SD
Timepoint Comparison
E
No parasites
X-Y magnitude (nm)
Force (pN)
3SD
Timepoint Comparison

Figure 7

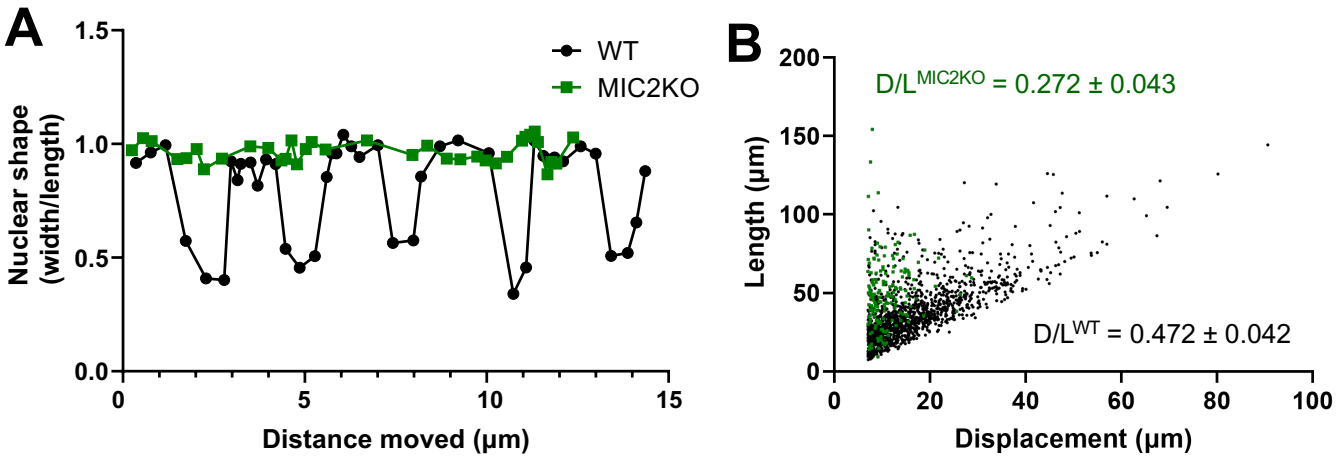
A
1.5
1.0
0.5
0.0
Nuclear shape (width/length)
0
5
10
15
Distance moved (µm)
WT
MIC2KO
B
200
150
100
50
0
Length (µm)
0
20
40
60
80
100
Displacement (µm)
D/L^MIC2KO = 0.272 ± 0.043
D/L^WT = 0.472 ± 0.042